Bioactive Materials 25 (2023) 594–614

Contents lists available at ScienceDirect

Bioactive Materials

journal homepage: www.keaipublishing.com/en/journals/bioactive-materials

Graphene oxide/gallium nanoderivative as a multifunctional modulator of osteoblastogenesis and osteoclastogenesis for the synergistic therapy of implant-related bone infection

Ying Yang [a,b,d,*], Min Li [c], Bixia Zhou [a,d], Xulei Jiang [a,d], Dou Zhang [b], Hang Luo [b,**]

[a] Department of Plastic Surgery, Xiangya Hospital, Central South University, Changsha, 410008, China
[b] State Key Laboratory of Powder Metallurgy, Central South University, Changsha, 410083, China
[c] Department of Oncology, Changsha Central Hospital, University of South China, Changsha, 410006, China
[d] National Clinical Research Center for Geriatric Disorders, Xiangya Hospital, Central South University, Changsha, 410008, China

ARTICLE INFO

Keywords:
Nanocomposites
Antimicrobial potency
Implant-associated bone infections
Osteogenesis
Osteoclastogenesis

ABSTRACT

Currently, implant-associated bacterial infections account for most hospital-acquired infections in patients suffering from bone fractures or defects. Poor osseointegration and aggravated osteolysis remain great challenges for the success of implants in infectious scenarios. Consequently, developing an effective surface modification strategy for implants is urgently needed. Here, a novel nanoplatform (GO/Ga) consisting of graphene oxide (GO) and gallium nanoparticles (GaNPs) was reported, followed by investigations of its *in vitro* antibacterial activity and potential bacterium inactivation mechanisms, cytocompatibility and regulatory actions on osteoblastogenesis and osteoclastogenesis. In addition, the possible molecular mechanisms underlying the regulatory effects of GO/Ga nanocomposites on osteoblast differentiation and osteoclast formation were clarified. Moreover, an *in vivo* infectious microenvironment was established in a rat model of implant-related femoral osteomyelitis to determine the therapeutic efficacy and biosafety of GO/Ga nanocomposites. Our results indicate that GO/Ga nanocomposites with excellent antibacterial potency have evident osteogenic potential and inhibitory effects on osteoclast differentiation by modulating the BMP/Smad, MAPK and NF-κB signaling pathways. The *in vivo* experiments revealed that the administration of GO/Ga nanocomposites significantly inhibited bone infections, reduced osteolysis, promoted osseointegration located in implant-bone interfaces, and resulted in satisfactory biocompatibility. In summary, this synergistic therapeutic system could accelerate the bone healing process in implant-associated infections and can significantly guide the future surface modification of implants used in bacteria-infected environments.

1. Introduction

Despite significantly improved technology of medical sterilization and asepsis, bacterial infections and bone osteolysis caused by infection remain great challenges in repairing severe bone fractures or defects in orthopedic or plastic surgeries [1]. Bacterial invasion characterized by colonization or even biofilm formation in wounded regions could unavoidably contribute to implant failure, resulting in substantial costs to society and patient morbidity [2,3]. Conventional implants without antimicrobial properties are vulnerable to biocontamination, which may provide a foothold for the rapid growth of adhered bacterial cells [2]. More importantly, continuous infections surrounding implants most frequently cause osteomyelitis. Implant-related osteomyelitis is mainly generated from *S. aureus* or *S. epidermidis* infections and is characterized by serious inflammation of bone and bone marrow [4,5]. Osteomyelitis is anticipated to produce devastating complications, such as prosthetic loosening and bone necrosis, during the rehabilitation of patients with bone injury, especially diabetic patients [6]. Considering the substantial financial burden and health concerns originating from implant-associated osteomyelitis, the development of anti-infection strategies for clinically used implants in patients at a high risk of bacterial invasion is urgently needed.

Peer review under responsibility of KeAi Communications Co., Ltd.
* Corresponding author. Department of Plastic Surgery, Xiangya Hospital, Central South University, 87 Xiangya Road, Changsha, 410008, Hunan, PR China.
** Corresponding author. State Key Laboratory of Powder Metallurgy, Central South University, 932 South Lushan Road, Changsha, 410083, Hunan, China.
E-mail addresses: forever_yang@csu.edu.cn (Y. Yang), hangluo@csu.edu.cn (H. Luo).

https://doi.org/10.1016/j.bioactmat.2022.07.015
Received 8 April 2022; Received in revised form 24 June 2022; Accepted 12 July 2022
Available online 21 July 2022

It is common practice to remove bacteria-infected implants and proceed with radical debridement and systemic application of antibiotics for the clinical treatment of implant-related osteomyelitis [7]. However, these typical treatments could contribute to antibiotic resistance, recurrence of bacterial colonization and compromised patient compliance [6,8]. Due to the increased complications and morbidity originating from implant-related osteomyelitis, extensive attention has been given to developing therapeutic strategies, such as clinically used antibiotic-loaded cements and scaffolds and nonantibiotic-incorporated local delivery systems in metal implants or bioceramic scaffolds [9]. Considering the large number of patients requiring metal implants in orthopedic or plastic clinics, the local delivery of antimicrobial agents by coating modification exhibited effective outcomes and promising prospects [9]. Currently, titanium implants supplemented with heavy metals or modified with micro/nanopatterned surfaces offer alternative platforms for tuning the biological properties of implants [10–14]. Nevertheless, relatively few studies focused on osteolysis and bone resorption, which are mainly caused by activated osteoclast differentiation and inflammatory reactions in bone infection models [15,16]. Consequently, an effective therapeutic approach to mitigate bacterial infection-associated bone loss is of vital importance to the successful osteointegration of implants in an infectious microenvironment.

Nowadays, graphene oxide (GO)-based nanomaterials are extensively employed in biomedical fields, such as tissue engineering, medical device coatings, diagnostic tools, local drug delivery for antineoplastic or antimicrobial purposes, and personal protective equipment [17,18]. Various antibacterial and osteopromotive strategies centered on GO-based nanocomposites have been developed due to their unique nanostructure and satisfactory biocompatibility and designability [18,19]. The antimicrobial actions of GO nanosheets is mainly attributed to oxidative stress-associated membrane destruction [20]. In addition, GO nanosheets have clear osteogenic and angiogenic properties, leading to reliable anti-infective and osteoconductive capacities for local therapy of implant-related bone infection [21,22]. Gallium (Ga) is a semimetallic element that exhibits antitumor, antiresorptive, and anti-inflammatory properties, rendering it an ideal candidate for the treatment of Paget's disease, myeloma and malignancy with hypercalcemia [23,24]. Moreover, Ga ions (Ga^{3+}) demonstrate high chemical similarity with ferric ions (Fe^{3+}); thus, Ga^{3+} could interfere with ferric iron-dependent metabolic pathways in bacteria [25]. It has been widely accepted that microbes possess unique iron-acquisition systems to obtain iron from the host environment, and the reduction of Fe^{3+} to Fe^{2+} is a critical process for intracellular metabolism, which is closely related to bacterial survival, colonization and pathogenicity [26]. Therefore, such a "Trojan horse" antimicrobial strategy appears to have no susceptibility to the classical resistance mechanisms commonly found in antibiotics [26], offering evident advantages over commercially available antibiotics against multidrug-resistant pathogens.

In addition, Ga exhibits a high affinity to growing or remodeling bone tissues and has inhibitory effects on RANKL-induced osteoclast differentiation through the downregulation of NFATc1 expression without negatively affecting osteoblasts [27]. Thanks to its chemical affinity to biological hydroxyapatite and excellent antiresorptive capability, Ga was reported to be a relevant and promising candidate for the local treatment of bone metastases and osteoporotic bone defects [28,29]. However, the administration of Ga failed to significantly affect the gene expression of markers in osteoblast differentiation, such as alkaline phosphatase activity and osteocalcin [27,30]. In addition, there is still a contradictory cytotoxicity towards osteoblast activity caused by Ga [27,29], and the results and conclusions summarized from these studies seem inconsistent due to the application of different manufacturing techniques, experimental procedures and cell lines. In consideration of the demands of osteoconductivity involved in implant-bone interfaces, substances, such as GO nanosheets, with good osteogenic potential may be suitable for improving therapeutic outcomes in implant-related osteomyelitis. More importantly, bacterial infection-induced inflammation could inevitably undermine the immune microenvironment, and osteoclasts could be a hotbed for *S. aureus* to grow and mature [31]. Increasing evidence suggests that several signaling pathways, such as the MAPK, Smad, Akt and NF-κB pathways, are involved in bacterial infection-induced osteomyelitis [31–34]. Relatively abundant levels of proinflammatory factors, such as IL-1α, IL-6, IL-17 and TNF-α, were found in *S. aureus*-infected femurs, and secreted bacterial factors from *S. aureus* have been found to facilitate RANKL-induced osteoclast differentiation and enhance trabecular bone loss through the MyD88/IL-1R signaling pathways [35]. Based on the aforementioned biological effects of GO and Ga along with the pathogenesis of osteomyelitis, it hypothesized that the combined application of GO nanosheets and Ga nanoparticles could ameliorate bacterial infection-triggered osteoclastogenesis and improve osteointegration by regulating relevant signaling pathways, which remains to be further clarified in this study.

Here, an ingenious strategy to couple antibacterial potency with the osteoinductive and antiresorptive potential of GO nanosheets and Ga nanoparticles was reported to eliminate biofilm formation, mitigate osteolysis and simultaneously improve osteointegration under an implant infection-related osteomyelitis scenario (Scheme 1). GO/Ga nanocomposites were prepared by modified low-temperature ultrasonic emulsification and *in situ* deposition methods. The *in vitro* antimicrobial potency, potential bacterium inactivation mechanisms, cytocompatibility and regulatory effects on osteoblast and osteoclast differentiation of these nanocomposites were systematically investigated after preliminary optimization of their biological activities. Furthermore, the relevant molecular mechanisms involved in osteoblastogenesis and osteoclastogenesis were explored and confirmed. Eventually, an *in vivo* infectious microenvironment in femurs was established to determine the therapeutic efficacy and biosafety of GO/Ga nanocomposites. Our results provide a potentially effective strategy to prepare GO/Ga nanoderivative-coated implants with great application prospects in accelerating the infectious bone healing process in implant infection-related osteomyelitis.

2. Materials and methods

2.1. Synthesis of graphene oxide/gallium (GO/Ga) nanocomposites

The GO/Ga nanocomposites were creatively manufactured using a modified low-temperature ultrasonic emulsification method as previously reported [36,37]. Briefly, 100 mg of metallic gallium (99.999% metals basis, Aladdin, Shanghai, China) were heated at 40 °C for 30 min to acquire a homogeneous liquid state, and 50 mL of ethylene glycol (spectroscopic purity ≥99%, Aladdin, Shanghai, China) were slowly added to the liquid gallium to serve as a dispersion stabilizer during nanocrystallization. Then, the mixture was ultrasonically irradiated by an ultrasonic transducer with a 13-mm tip (VC500, 20 kHz, 500 W; Sonics and Materials Inc., Newtown, CT, USA) in a pure N_2 atmosphere and reflux for approximately 2 h, and the Ga nanoparticles (GaNPs) were obtained after centrifugation. In this study, graphene oxide (GO) was prepared using a modified Hummers' method as previously reported [38]. The desired amount of GO powder (100 mg) was added to an ethyleneglycolic suspension (50 mL, Aladdin) containing 100 mg of GaNPs with an additional ultrasonication treatment for *in situ* deposition under the same condition, followed by centrifugation, washing and drying to obtain desired GO/Ga nanocomposites (mass ratio = 1:1). In addition, GO/Ga nanocomposites with mass ratios of 1:0.5 and 1:2 were prepared in a similar manner, and GO and GaNPs were prepared and served as controls.

2.2. Surface characterizations

Transmission electron microscopy (TEM) images of the GO and GO/Ga nanocomposites were obtained using a Tecnai G_2 F20 electron microscope (200 kV, JEM-2100F, JEOL Ltd., Tokyo, Japan). Meanwhile,

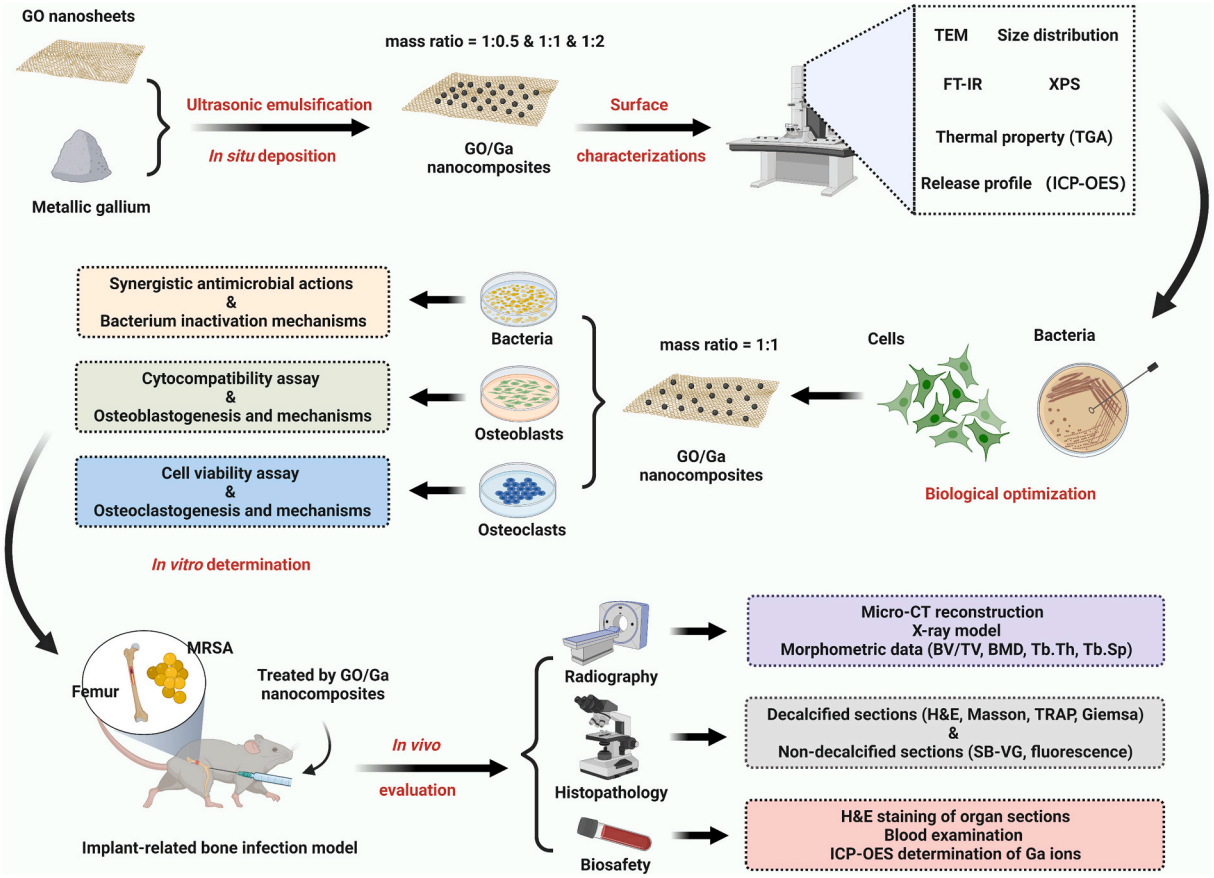

Scheme 1. Schematic illustration of the experimental design and procedures (Created with BioRender.com).

the size distribution of the GaNPs was analyzed using ImageJ software (NIH, Maryland, USA). The distribution of functional groups grown on the nanocomposites was analyzed by Fourier transform infrared spectroscopy (FT-IR, Nicolet iS5, Thermo Fisher Scientific, MA, USA) and X-ray photoelectron spectroscopy (XPS, EscaLab Xi+, Thermo Fisher Scientific). FT-IR spectra with a resolution of 4.0 cm^{-1} were obtained from 32 scans of each sample ranging from 4000 to 400 cm^{-1}. The excitation source of XPS was an Al Kα with 1486.6 eV at a voltage of 12.5 kV and electricity of 16 mA. The thermal property of the prepared nanocomposites was investigated by a thermogravimetric (TG) analyzer (DTA-7300, SEIKO Ltd., Tokyo, Japan) with a heating rate of 20 °C/min from 20 to 1000 °C.

2.3. Cumulative release profile of Ga^{3+} from nanocomposites

The release property of GO/Ga nanocomposites was determined in phosphate buffered saline (PBS, pH = 7.4, HyClone, Thermo Fisher Scientific) at 37 °C under orbital shaking at 100 rpm for up to 12 days [39]. The solutions were removed every day from Days 0–12, and the incubation solutions were refreshed accordingly. The released gallium ions (Ga^{3+}) at each interval were further determined by inductively coupled plasma-optical emission spectrometry (ICP-OES, PerkinElmer, Optima 5300 DV, USA) to confirm the cumulative release profile of Ga^{3+} from the nanocomposites. In addition, the loading efficiency of Ga in each GO/Ga nanocomposite was confirmed by ICP-OES after the samples were absolutely dissolved in a strong acid solution.

2.4. Optimization of the antibacterial potency and cytocompatibility of the nanocomposites

2.4.1. Preparation of bacteria and cells

To determine the optimal GO/Ga nanocomposite to be used in the subsequent *in vitro* and *in vivo* biological experiments, methicillin-susceptible *S. aureus* (ATCC25923), *Escherichia coli* (ATCC 25922) and methicillin-resistant *S. aureus* (ATCC43300), representing typical gram-positive, gram-negative and antibiotic-resistant bacterial strains, respectively, were used to compare the antibacterial efficacy of different GO/Ga nanocomposites. The resurgent bacteria (1×10^8 CFU/mL) were suspended in Mueller-Hinton broth (MHB, Solarbio, Beijing, China) for the microbiological experiments [21]. Meanwhile, primary bone mesenchymal stem cells (BMSCs) isolated from rats as previously described were applied to assess the cytocompatibility of different GO/Ga nanocomposites [40]. rBMSCs of passages two to three ($P_{2/3}$) and MC3T3-E1 and RAW 264.7 (1×10^8 cells/mL) suspended in α-MEM (HyClone) supplemented with 15% fetal bovine serum (FBS, Gibco, Thermo Fisher Scientific) and 100 IU/mL streptomycin/penicillin (HyClone) were prepared for the subsequent cytological experiments.

2.4.2. Comparative analysis of the antimicrobial potency and cytocompatibility of GO/Ga nanocomposites

To compare the *in vitro* antibacterial efficacy of different GO/Ga nanocomposites, the minimum inhibiting concentrations (MICs) of the nanomaterials against the three tested bacterial strains was examined according to a previous protocol [41]. Then, 1 mL of bacterial cells (1×10^7 CFU/mL) was inoculated in MHB medium containing the aforementioned nanomaterials at the indicated concentrations (20, 40 and 80 μg/mL), followed by incubation for 6 h at 37 °C. The metabolic activities of the bacterial cells after coculture were analyzed by resazurin

staining (AlamarBlue™ Cell Viability Reagent, Thermo Fisher Scientific), which is regarded as a reliable method to quantify viable bacterial cells [42]. After the incubation, 100 μL of the cultures in each group and 10 μL of cell viability reagent were added to the wells, followed by an additional incubation at 37 °C for 3 h. The mixed solutions was measured at 570 nm (OD_{570}) on a microplate reader (Infinite M200 PRO, TECAN, Männedorf, Switzerland). Similarly, the viability of rBMSCs, MC3T3-E1 and RAW 264.7 (1×10^5 cells/well) treated with various nanomaterials for 12 h was also examined by a cell counting kit-8 (CCK-8, Dojindo Molecular Technologies Inc., Kumamoto, Japan) assay [21], and OD_{450} values of the mixed solutions were confirmed after 3 h of incubation at 37 °C.

2.5. Synergistic antibacterial activity of GO/Ga nanocomposites

2.5.1. Bactericidal effects

The bactericidal effects of the GO/Ga nanocomposites (mass ratio = 1:1) were first determined using the spread plate method [21]. Briefly, 500 μL of bacterial suspension (5×10^6 CFUs) were inoculated in MHB medium containing various nanomaterials (GO, GaNPs and GO/Ga, 40 μg/mL) for 4 h, and gradient dilutions of each culture were plated onto tryptic soy agar (TSA) for another 24 h incubation. The number of live bacterial cells in the above cultures was counted, and the bacterial colonies in each group were normalized to those found in the controls. Then, Kirby-Bauer antibiotic testing (agar disk diffusion method) was employed to further confirm the antimicrobial efficacy of the nanomaterials against the three bacterial strains [43]. Prepared bacterial cells (1×10^8 CFU/mL) were evenly plated onto TSA dishes, and customized Oxford cups containing 250 μL of nanomaterials (GO, GaNPs and GO/Ga, 40 μg/mL) were placed vertically, followed by a 24 h incubation at 37 °C. The antimicrobial efficacy of the nanomaterials against the tested strains was determined by measuring the inhibition zones as previously described [43,44].

2.5.2. Evaluation of the integrity of the bacterial membrane

Adenosine triphosphate (ATP) and potassium ion (K^+) leakage assays were used to further evaluate the integrity of the bacterial membrane, thus providing more direct evidence of the synergistic bactericidal effects of the GO/Ga nanocomposites. In brief, 500 μL of bacterial suspension (1×10^7 CFUs) were inoculated in MHB medium containing various nanomaterials (GO, GaNPs and GO/Ga, 40 μg/mL) for up to 6 h. The ATP and K^+ released into the supernatant of each culture were collected after centrifugation at the desired time points (30, 60, 120 and 360 min). The leakage of ATP from the inner membrane of the bacterial cells was examined by a luminometer (TECAN) after being cocultured with the indicated volume of a BacTiter-Glo™ Microbial Cell Viability Kit (Promega Corporation, Madison, USA) according to the provided protocols. In addition, the released K^+ in the supernatant from each culture was determined by ICP-OES (PerkinElmer) as mentioned above.

2.5.3. Morphological analysis of bacteria by microscopy

In order to acquire a deeper comprehension regarding the synergistic antimicrobial actions and potential mechanism of GO/Ga nanocomposites, morphoplogical analysis of bacteria was conducted by scanning electron microscopy (SEM) and TEM. As indicated above, 500 μL of bacterial suspension (ATCC25922 and ATCC25923, 1×10^8 CFUs) were inoculated in 5 mL of MHB medium containing different nanomaterials (GO, GaNPs and GO/Ga, 40 μg/mL) for 6 and 24 h, and 1 mL of sample containing bacteria and nanomaterials was extracted from suspensions after incubation at indicated time points. To obtain SEM images, samples were fixed successively with 2.5% glutaraldehyde solution and 1% osmic acid for 12 and 1 h, respectively, followed by a sequential dehydration with 30, 50, 70, 80, 90, 95 and 100% of ethanol solutions for 15 min each time. Then, samples were air-dried and sputter-coated with gold and examined by a SEM (SU8010, HITACHI, Tokyo, Japan) with an accelerating voltage of 3 kV. To further observe the morphological changes of bacteria by TEM, samples were fixed and dehydrated as similar as the SEM imaging, and finally dehydrated them with pure acetone for 20 min. The dehydrated samples were placed in mixed embedding agents and polymerized at 70 °C for 24 h. Finally, slices with thickness of 90 nm were prepared on an ultramicrotome (Leica UC7, Leica Microsystems, Wetzlar, Germany), and examined on a HT7800 TEM (HITACHI) operating at an accelerating voltage of 80 kV.

2.6. Determination of cytocompatibility with osteogenic cells

In order to determine the oxidative stress of the rBMSCs reacting to the tested nanomaterials, an oxidation sensitive fluorescent probe, 2′, 7′-ichlorofluorescin-diacetate (DCFH-DA), was applied to clarify the reactive oxygen species (ROS) levels inside the cells according to our previously reported protocols [45]. Briefly, 1 mL of rBMSCs (1×10^6 cells) were added to culture dishes specifically for confocal laser scanning microscope (CLSM, Leica TCS SP8, Leica Microsystems) observation, followed by an additional cocultured with nanomaterials with indicated concentrations (40 μg/mL) for 24 h. Cells were stained with DCFH-DA for nearly 1 h and images were obtained after scanning. Then, the cell viability was evaluated by a Live/Dead Cell Kit (Abcam, Cambridge, UK) by means of flow cytometry as previously confirmed [46]. Briefly, rBMSCs (1×10^6 cells/well) were cocultured with various nanomaterials (40 μg/mL) for 24 h and then were suspended in 5 mL of PBS, followed by a centrifugation for 5 min. Cells were stained with 100 μL of combination dye for 15 min and washed by PBS for two times to remove non-specific staining, and the stained samples were simultaneously analyzed by flow cytometry (BD LSRFortessa, BD Biosciences, San Jose, CA, USA). Data regarding cell apoptosis was processed by FlowJo software (TreeStar, Ashland, OR, USA). Subsequently, rBMSCs cocultured with nanomaterials were fixed by 4% paraformaldehyde for approximately 15 min, then cells were treated with 0.1% TritonX-100 solution for 10 min to increase the permeability of cell membranes and washed again by PBS for three times. The filamentous actin of the cytoskeleton and the nuclei of tested rBMSCs were sequentially stained with TRITC (rhodamine)-phalloidin (Thermo Fisher Scientific) and 4′,6-diamidino-2-phenylindole (DAPI, Sigma-Aldrich) for 15 min and 45 min, respectively. The filamentous actin of the cytoskeleton of rBMSCs were also visualized by CLSM. To further confirm the oxidative stress of rBMSCs (1×10^6 cells/well) after treatment with various nanomaterials for 24 h, the levels of ROS and lactate dehydrogenase (LDH) in the culture superntants were also confirmed by an enzyme-linked immunosorbent assay (ELISA) kit (Shanghai Hufeng Chemical Co., Ltd, Shanghai, China), and OD_{450} values were recorded. In the end, cell proliferation of rBMSCs (5×10^4 cells/well) was evaluated by CCK-8 assay after 1, 3 and 5 d of coculture as described above, and the absorbance values of each group at 3 and 5 d were normalized to those at 1 d.

2.7. In vitro effects of GO/Ga nanocomposites on osteoblastogenesis

2.7.1. Cell culture and osteoblast differentiation

As previously indicated, rBMSCs (5×10^5 cells/well) were cocultured with different nanomaterials (40 μg/mL) in 12-well plates. The culture medium was replaced by OriCell osteogenic inductive medium (RASMX-90021, Cyagen Biosciences, Inc., USA) after 24 h of incubation [47]. The osteogenic inductive medium was refreshed every 2 d.

2.7.2. Alkaline phosphatase (ALP) staining and quantification

rBMSCs were treated with the *ALP* staining method after 10 and 14 d of culture with osteogenic inductive medium as previously reported, and plates containing stained rBMSCs were photographed under a microscope (Leica Microsystems) [48]. Then, the *ALP* activity was confirmed by an *ALP* microplate test kit (Solarbio), and OD_{510} values were recorded and compared. The absorbance of each group was normalized to the corresponding total protein content as confirmed by a

BCA Protein Assay Kit (Thermo Fisher Scientific).

2.7.3. Alizarin red S (ARS) staining and quantification

The mineralization of tested rBMSC was evaluated by Alizarin red staining after 21 and 28 d of osteogenic induction [48]. Cells were stained with 1% alizarin red solution (Cyagen Biosciences) for 30 min after being fixed with 4% paraformaldehyde (PFA, Solarbio). Images of the stained cells were collected by optical microscopy (DM2000, Leica Microsystems). Then, the stained cells were treated with 10% cetylpyridinium chloride in 10 mM sodium phosphate (Sigma-Aldrich), followed by the measurement of OD_{620} values.

2.7.4. Expression of osteogenic differentiation-associated genes

Real-time polymerase chain reaction (RT-PCR) was used to investigate the mRNA expression of osteoblastogenesis-related markers, including alkaline phosphatase (*ALP*), osterix (*OSX*), osteocalcin (*OCN*) and osteopontin (*OPN*) [46,49]. The total RNA was obtained from induced cells cocultured with nanomaterials (40 μg/mL) at 6 and 12 d using TRIzol reagent (Invitrogen, Thermo Fisher Scientific) following the manufacturer's protocol. The total RNA concentration was determined by a NanoDrop spectrophotometer (ND-1000, Thermo Fisher Scientific), and cDNA templates were synthesized from the extracted RNA using a PrimeScript™ RT reagent kit (Takara Bio Inc., Dalian, China). Finally, quantitative RT-PCR was performed with a QuantStudio™ 7 Flex Real-Time PCR System (Applied Biosystems, Thermo Fisher Scientific) using a TB Green® Premix Ex Taq™ II kit (Takara). The sequences of the forward and reverse primers were synthesized by Sangon Biotech Ltd., Shanghai, China and are shown in Table S1. The housekeeping gene glyceraldehyde-3-phosphate dehydrogenase (*GAPDH*) was used as an internal control, and the transcript levels of the genes were normalized to that of *GAPDH*.

2.8. In vitro effects of GO/Ga nanocomposites on osteoclastogenesis

2.8.1. Cell culture and osteoclast differentiation

In this study, primary bone marrow macrophages (rBMMs) isolated from the bone marrow of rats and RAW 264.7 cells were employed to determine the biological effects of different nanomaterials (40 μg/mL) on osteoclastogenesis according to previous studies [50,51]. rBMMs or RAW 264.7 cells were cultured in α-MEM supplemented with 1% penicillin/streptomycin, 15% FBS and 25 ng/mL recombinant rat M-CSF (Sigma-Aldrich, USA) or mouse M-CSF (R&D Systems, Minneapolis, MN, USA) for 24 h and then transferred into an incubator for an additional 3–5 d of culture to achieve sufficient confluence. rBMMs (1×10^5 cells/well) were seeded into 96-well plates and treated with the indicated concentration of nanomaterials (GO, GaNPs and GO/Ga) supplemented with indicated concentration of recombinant rat (Sigma-Aldrich) or mouse (R&D Systems) RANKL (50 ng/mL) and corresponding M-CSF (25 ng/mL).

2.8.2. Cell viability assay

The apoptotic effect of different nanomaterials at the indicated concentration (40 μg/mL) on rBMMs was confirmed by flow cytometry. rBMMs (5×10^5 cells/well) were seeded into 12-well plates for 24 h of culture and then treated with the desired nanomaterials for up to 48 h. A flow cytometric analysis was performed after the rBMMs were treated with an Annexin V-FITC Detection Kit (BD Biosciences) [52]. In brief, rBMMs were suspended in 500 μL of 1 × binding buffer. Then, 10 μL of Annexin V-FITC and propidium iodide (PI) (BD Biosciences) were sequentially added to the suspension, and the solution was incubated on ice for 30 min away from light. The cells were collected and resuspended in 100 μL binding buffer for further analysis using a flow cytometer (BD LSRFortessa, BD Biosciences). The cell apoptosis data were analyzed by FlowJo software (TreeStar) as mentioned above, and the proportion of apoptotic cells in each group was confirmed.

2.8.3. Evaluation of tartrate-resistant acid phosphatase (TRAP) activity

After 5 d of coculture with different nanomaterials, mature osteoclasts were fixed by 4% PFA (Solarbio) in PBS for 20 min. Then, the cells were stained with an Acid Phosphatase Assay Kit (TRAP, Sigma-Aldrich) to determine TRAP activity in accordance with the manufacturer's instructions. Images of the stained cells were obtained by optical microscopy (Leica Microsystems). Furthermore, the area and number of TRAP-positive cells representative of differentiated multinucleated osteoclasts were quantified in randomly selected fields of view in each group.

2.8.4. Expression of osteoclastogenesis-associated genes

Analogously, the expression of genes closely associated to osteoclast differentiation, including *TRAP*, calcitonin receptor (*CTR*), cathepsin K (*CtsK*) and nuclear factor of activated T cells (*NFATc1*), was confirmed by RT-PCR at 1, 3 and 5 d. The sequences of the forward and reverse primers were synthesized by Sangon Biotech Ltd., Shanghai, China and are shown in Table S1. *GAPDH* was used as an internal control, and the results are shown as relative expression values normalized to *GAPDH*.

2.9. Investigation of the potential molecular mechanisms involved in osteoblastogenesis and osteoclastogenesis

2.9.1. Western blot analysis

In this study, a western blot assay was used to confirm the potential signaling pathways concerning the regulatory effects of the GO/Ga nanocomposites on the osteoblasts (MC3T3-E1 cells) and osteoclasts (RAW 264.7 cells) differentiation as previously described [53]. For the investigation of osteoblastogenesis, the total proteins of the cells were collected by radioimmunoprecipitation assay (RIPA) reagent (Sigma-Aldrich) after 7 d of coculture with different nanomaterials in osteogenic inductive medium. For the investigation of osteoclastogenesis, RAW 264.7 cells were pretreated with indicated concentration of nanomaterials for 4 h, and the total proteins of the cells were obtained after 30 min or 3 d of coculture with different nanomaterials in medium supplemented with 50 ng/mL of RANKL. To further confirm the crucial role of corresponding signaling axis involved in the osteogenic and osteoclast differentiation, a small interfering RNA (siRNA) mediated BMP-2 gene knockdown (Ribobio, Guangzhou, China), and specific activators of JNK (Anisomycin, 50 μM, S7409), P38 (Asiatic acid, 10 μM, S2266) and NF-κB (Betulinic acid, 15 μM, S3603) purchased from Selleck Chemicals (Houston, USA) with indicated concentration were used to perform reverse validation experiments aimed at verifying the stimulative effects of GO/Ga nanocomposites on BMP/Smad signaling pathways and the inhibitory effects on MAPK and NF-κB signaling pathways, as previously reported [53–56]. The prepared samples were transferred to polyvinylidene difluoride (PVDF) membranes (Millipore, MA, USA) after being separated by 10% sodium dodecyl sulfate-polyacrylamide gel electrophoresis (SDS-PAGE, Sigma-Aldrich). Then, the transferred membranes were incubated with primary antibodies against *p*-Smad 1/5, Smad-1, Smad-5, *p*-JNK, JNK, *p*-ERK, ERK, p-P38, P38, *p*-IkBα, IkBα, p-P65, P65, NFATc1 and c-Jun (1:1000, Cell Signaling Technology, MA, USA) for nearly 12 h at 4 °C and incubated again with fluorescent-based anti-rabbit or mouse IgG secondary antibody (1:2000, Cell Signaling Technology) for approximately 1 h in the dark, followed by several rinses with TBST (5% skimmed milk in Tris-buffered saline supplemented with 0.2% Tween 20). An infrared imaging system (Odyssey, LI-COR, Nebraska, USA) was used to perform the scan and analysis of the prepared immunoreactive bands. A β-actin antibody (1:1000, Cell Signaling Technology) was used as a control. The gray values of the tested bands were calculated and normalized to β-actin as confirmed by ImageJ software (NIH, USA).

2.9.2. Luciferase reporter gene activity

To further confirm the regulatory effects of the GO/Ga nanocomposites on the expression of BMP-2 and NFATc-1, luciferase reporter

gene assessments based on MC3T3-E1 and RAW264.7 cells that were stably transfected with BMP-2 and NFATc-1 luciferase reporter constructs, respectively, were performed as previously indicated [53]. Briefly, the cells were transfected with Lipofectamine™ 3000 Transfection Reagent (Thermo Fisher Scientific) according to the provided protocols. BMP-2 or NFATc-1 promoter-luciferase reporter constructs containing the corresponding sequences cloned in front of the Gaussia luciferase gene were customized and purchased from Genecopoeia (MD, USA). Stably transfected cells were treated with different nanomaterials for 6 h with specific stimulations, and the luciferase activities were confirmed by a Pierce™ Gaussia Luminescence Assay Kit (Thermo Fisher Scientific) following the manufacturer's instructions. In addition, the luciferase activities were normalized to that of the vehicle control.

2.9.3. Molecular docking

Recently, computational molecular docking analyses have been shown to provide valuable information regarding the interaction between biologically active molecules and their targets [57]. Thus, in this study, the binding affinity of Ga^{3+} toward certain amino acids target proteins as mentioned above was confirmed by constructing three-dimensional homology models of mouse JNK1, JNK2 and P38α kinase domains with Modeler-v9.22 using the architectures of human JNK/P38 as templates. The stereochemical quality and structures of the JNK/P38 models were further verified by PROCHECK based on AutoDock VINA, and the Lamarckian genetic algorithm was utilized to link Ga^{3+} with JNK1/2 and P38α kinases [58]. Images of molecular docking demonstrating binding activity were prepared using PyMOL visualization software (Schrödinger LLC, NY, USA).

2.10. In vivo therapeutic efficacy in implant-related bone infection

2.10.1. Establishment of an animal model

To investigate the *in vivo* therapeutic efficacy of GO/Ga nanoderivatives, a modified implant-related bone infection model was established and systematically evaluated through a radiographic and histopathological analysis based on previous studies [59,60]. The design and methods of this study were reviewed and approved by the Laboratory Animal Welfare and Ethical Committee of Central South University (No. 2022sydw002). Twenty-four eight-week-old male SD rats weighing 200–250 g were purchased from Hunan Slac Laboratory Animal Co., Ltd. (Slac, Changsha, China). In the present study, the following four independent groups (n = 6) were established (Table S2): 1) uninfected group (Group U); 2) infected group (Group I); 3) infected group with the administration of GO/Ga nanocomposites (Group IGG); and 4) uninfected group with the administration of GO/Ga nanocomposites (Group UGG). Rats were allowed to eat and drink ad libitum for 5–7 d prior to the surgery for the purpose of environmental adaptation. The rats received an intraperitoneal injection of pentobarbital sodium (1%, 80 mg/kg) for anesthetization. An approximately 2 cm long incision was made along the lateral side of the distal femur to dislocate the knee joint. After the identification of the intercondylar notch region of the knee, a drill with a diameter of 2.0 mm was percutaneously inserted into the femoral medullary cavity and advanced to a depth of 2.0 cm. A customized titanium rod implant measuring 1.5 mm in diameter and 15 mm in length was soaked in methicillin-resistant *S. aureus* (ATCC43300, 1×10^6 CFU/mL) for 10 min. Subsequently, the bacteria-contaminated implants were inserted into the femoral canal after normal saline washing. Two hundred microliters of PBS containing GO/Ga nanocomposites (mass ratio = 1:1, 40 μg/mL) were slowly injected into the intramedullary space, followed by closure of the drilled hole with bone wax and wounding with ETHICON sutures. Equivalent dose of GO/Ga nanocomposites were injected into the intramedullary space once a week for 3 w. On the day of sacrifice (5 w), the rats were intraperitoneally treated with an overdose of anesthetic (4% pentobarbital sodium), and the femurs were harvested and fixed in 4% paraformaldehyde for the subsequent micro-CT and histopathological examination.

2.10.2. Micro-CT assay

In this study, a high-resolution micro-CT (μCT 80, Scanco Medical, Brüttisellen, Switzerland) was adopted to perform the morphometric measurement of the harvested femurs from the rats in each group at the time of sacrifice (n = 5). The isometric resolution of the scanning was 20 μm with X-ray energy settings of 80 kV and 80 μA. The radiological images were obtained by the X-ray model of the manufacturer's processing software. Overall, three-dimensional images of the femur were recorded, and then, longitudinal and transverse sections from the region of interest (ROI) were reconstructed and analyzed. The following morphometric data of selected ROIs in the reconstructed sections were recorded as previously described: the bone volume/total volume (BV/TV), bone mineral density (BMD), trabecular thickness (Tb. Th), trabecular separation (Tb. Sp), number of porosities and percentage of total porosity [61].

2.10.3. Histopathological examination

Bone infection, osteolysis and osseointegration in each group (n = 6) were histopathologically evaluated on the day of sacrifice using various section stainings. In addition, fluorescent labeling of the newly formed bone tissues around the bone-implant interfaces was confirmed at week 5 after surgery by an intraperitoneal injection of calcein green (15 mg/kg, Sigma-Aldrich) [62]. Histological sections were obtained and divided into decalcified (n = 3) and nondecalcified (n = 3) slices. Femurs containing implants were dehydrated by gradient ethanol and then embedded in methylmethacrylate (MMA) for two weeks to realize satisfactory infiltration and polymerization. The sections were ground to approximately 50 μm thickness, followed by fluorescence imaging of newly formed mineralization and combined Stevenel's Blue and Van Gieson (SB-VG) staining as previously reported [15]. Images were captured and bone-implant contact (BIC) of longitudinal sections from the femoral shaft and transverse sections from the femoral condyle was recorded by Bioquant imaging software (Nashville, USA). Femurs without implants were embedded in paraffin after sufficient decalcification, and longitudinal or transverse sections at a thickness of 5 μm were also obtained. The bone morphology was observed after Hematoxylin and eosin (H&E) and Masson's trichrome staining. The active osteoclasts and residual bacteria were recorded via TRAP and Giemsa staining, respectively. Specifically, histopathological scores concerning relevant signs of bone infection were recorded by an experienced pathologist blinded to the grouping situation according to a modified scoring system [63].

2.10.4. Determination of in vivo biosafety

A histopathological analysis of the major organs and blood biochemical evaluation of blood samples were performed to determine the *in vivo* biosafety of GO/Ga nanocomposites according to previous studies [21,64]. Briefly, sections of the heart, lung, spleen, liver and kidney from the rats in each group (n = 4) were obtained and stained with an H&E staining kit for the observation of the organizational structure. In addition, blood samples taken from the caudal vein of the rats in each group (n = 4) were examined (routine blood examination, hepatic and renal function) according to the standard procedures of a laboratory organization for animal experiments. In addition, the content of Ga^{3+} in these organs was confirmed by ICP-OES after thorough tissue homogenization on the day of sacrifice [60].

2.11. Statistical analysis

In this study, the data are expressed as the mean ± standard deviation (mean ± SD) and were analyzed using Origin 8 (Origin Lab, MA, USA) or GraphPad Prism 5 software (GraphPad Software, CA, USA). After verification of the normal distribution and homogeneity of variance results, a one-way analysis of variance (ANOVA) or nonparametric

tests (Kruskal-Wallis H test) were utilized to perform the statistical analyses by means of SPSS software (version 24.0, IBM Corp, NY, USA). Statistical significance was confirmed when the *p*-value was less than 0.05.

3. Results and discussion

3.1. Surface characterization and release profile of Ga^{3+} from nanocomposites

Based on previously reported methods [36,37], gallium nanoparticles (GaNPs) were evenly distributed on the surface of GO nanosheets (Fig. 1a). Consistent with a previous study, the deposited GaNPs with a lattice spacing of 0.263 nm were crystalline as showing in the high-resolution TEM images [37]. Additionally, the size distribution of the GaNPs was 14.4 ± 3.0 nm (Fig. 1b). It is still a challenge to prepare Ga nanoparticles, and colloidal GaNPs are prone to agglomerate [36]. Considering the particularity of Ga nanoparticles, modified low-temperature ultrasonic emulsification and *in situ* deposition were used to prepare GO/Ga nanocomposites. It found that the GaNPs attached to the GO nanosheets were well separated, indicating that GO nanosheets could prevent the coalescence and agglomeration of GaNPs. It has been confirmed that GO nanosheets have many oxygen-containing groups including carboxyl (-COOH), hydroxy (-OH) and carbonyl groups (C═O) [20,21,38]. Therefore, it speculated that these functional groups of GO could provide ideal sites for the nucleation of GaNPs via

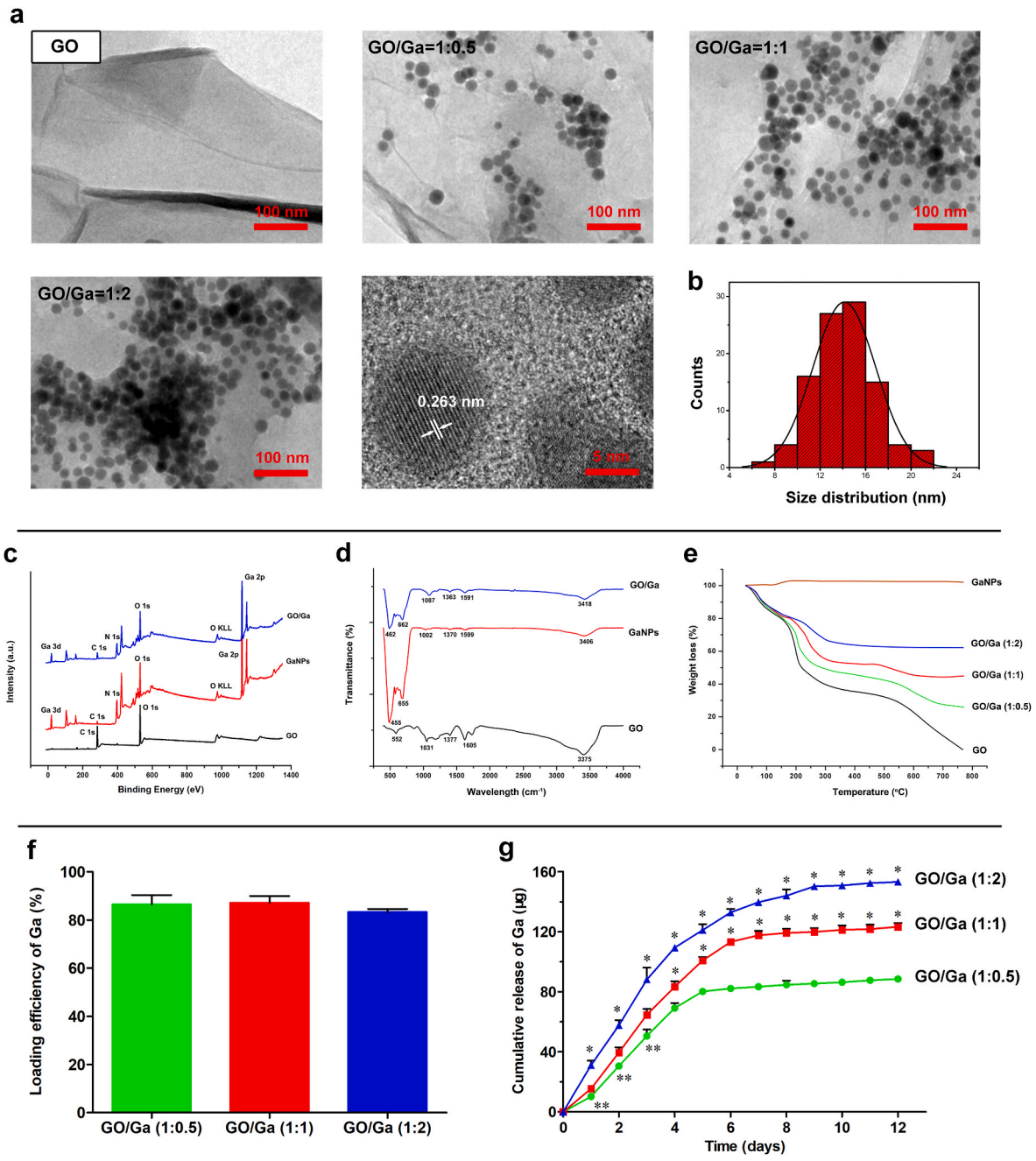

Fig. 1. Synthesis and characterization of GaNPs surface decorated on GO nanosheets. (a) TEM images. (b) Size distribution of GaNPs grown on GO nanosheets. (c) XPS survey spectra. (d) FTIR spectra. (e) Thermal properties of the nanomaterials confirmed by TGA. (f) Quantity of the loading efficiency of Ga with various incorporation ratios in GO/Ga nanocomposites. (g) Cumulative release behavior of gallium ions (Ga^{3+}) from the nanoderivatives within 12 d *p < 0.01 compared with the other groups, **p < 0.05 compared with GO/Ga (1:1).

electrostatic interactions, contributing to the stabilization and dispersibility of GaNPs grown on the surface of GO nanosheets.

XPS and FT-IR were used to confirm the chemical constitution and surface functional groups of the nanomaterials. As demonstrated in Fig. 1c, typical gallium photoelectron signals, such as a Ga 3d signal centered at 18.21 eV and a Ga 2p signal centered at 1117.81 eV, were exclusively found in GaNPs and GO/Ga, providing significant information regarding the chemical state (oxidation or valence numbers) of gallium in these nanomaterials [65]. In addition, the C–O or C–C bonds (C 1 s) representative of functional groups located at 282.53 eV were obviously found in the GO-containing nanomaterials. Furthermore, typical absorption bands, such as 1031 cm^{-1}, 1605 cm^{-1} and 3375 cm^{-1}, were recorded in the GO nanosheets and weakened in the GO/Ga nanocomposites as a result of the possible electrostatic interactions between the gallium and oxygen-containing groups (Fig. 1d). It was also clearly illustrated that the absorption peaks of GaNPs were found near 500 cm^{-1}, which may be assigned to the Ga–O stretching vibrations [66]. The thermal properties of these nanomaterials ranging from 20 to 1000 °C were investigated by TGA, as shown in Fig. 1e. Except for the GaNPs, a weight loss of approximately 17%–20% was observed in the GO nanosheets and GO/Ga nanocomposites below 150 °C because of water evaporation [21]. In contrast, a weight increase of approximately 5% was found in the GaNPs as a result of nanoparticle oxidation. Then, approximately 20%, 25%, 30% and 40% losses in weight in GO/Ga (1:2), GO/Ga (1:1), GO/Ga (2:1) and GO, respectively, were found between 150 °C and 300 °C caused by the cleavage of oxygenated functional groups. Accompanied by the continuous decomposition of the graphitic portion, approximately 5%, 10%, 25% and 40% losses in weight in GO/Ga (1:2), GO/Ga (1:1), GO/Ga (2:1) and GO, respectively, were found between 300 °C and 800 °C. Based on these findings, GO/Ga nanocomposites with the indicated mass ratio were successfully manufactured, and partial oxidation occurred during the detection process due to their unique sensitivity to oxygen and water in the air.

To determine the loading efficiency of the GaNPs in each GO/Ga nanocomposite, the samples were dissolved in a strong acid solution, followed by the quantity of the released Ga^{3+} using ICP- OES (Fig. 1f). Approximately 85% of Ga was converted into nanoparticles grown over the surface of GO nanosheets, and there were no significant differences among different GO/Ga nanocomposites ($p > 0.05$). Then, the cumulative release behavior of gallium ions (Ga^{3+}) from the GO/Ga nanocomposites within 12 d was confirmed using ICP-OES, as shown in Fig. 1g. There was an initial burst release of Ga^{3+} in all GO/Ga nanocomposites within 4 d, followed by a relatively slow release from 5 to 12 d. The release amount of the three groups collected from the indicated time points exhibited significant differences during the 12 d degradation as shown in Fig. 1g ($p < 0.01$ or $p < 0.05$). Interestingly, a small percentage of GaNPs was also found in the incubation solutions after the confirmation by TEM, indicating that the main forms of released gallium were GaNPs and Ga^{3+}, which is similar to the release behaviors of GO/Cu nanocomposites as previously confirmed [21]. Based on the quantitative analysis of the loading efficiency and cumulative release of Ga as described in Fig. 1f and Fig. 1g, it came to the conclusion that the release ratio of Ga elements from the GO/Ga (1:0.5), GO/Ga (1:1), GO/Ga (1:2) was approximately 77%, 71% and 69%, respectively, suggesting that nanocomposites with less content of Ga had greater release ratio after 12 d of *in vitro* degradation. A previous study found that both Ga nanoparticles and Ga ions derived from the dissolution of Ga nanoparticles were possible sources that contribute to the antibacterial action of GaNPs-based nanomaterials [36]. Consequently, both GaNPs and Ga^{3+} are expected to provide antimicrobial actions against microorganisms as discussed later.

3.2. Determination of GO/Ga nanocomposites with optimal biological performances

Considering the controversy regarding the selective bactericidal activity and mammalian cell cytotoxicity of GO-based nanomaterials [20], it is of great concern to optimize and balance the antimicrobial activity and cytocompatibility of the GO/Ga nanocomposites in advance of the subsequent investigations. Therefore, a comprehensive analysis of their biological performances was conducted (Fig. S1). The nanomaterials at the indicated concentrations (20–80 μg/mL) were incubated with the different bacterial strains and cell lines (rBMSCs, MC3T3-E1 and RAW 264.7) for 6 and 12 h, respectively. In addition, the MICs of these nanomaterials against the tested bacteria were confirmed and compared (Table S3). Overall, these nanomaterials had a concentration-dependent bactericidal effect, especially the GO/Ga nanocomposites. The antimicrobial efficacy of the GO/Ga nanocomposites improved as the gallium content increased. Our results demonstrate a synergistic antimicrobial effect of the combination of GO nanosheets and Ga nanoparticles, and the antibacterial efficacy was positively related to the incorporation ratio of gallium. In addition, the tested cell lines demonstrated relatively good viability after the incubation with all nanomaterials at concentrations of 20 and 40 μg/mL ($p > 0.05$). However, significantly increased cytotoxicity was found with these nanomaterials at a concentration of 80 μg/mL ($p < 0.05$).

GO nanosheets with relatively low concentrations could facilitate the adherence and proliferation of mammalian cells, whereas concentration-dependent cytotoxicity in mammalian cells was found with GO or graphene (>50 μg/mL) [67]. In this study, significantly increased cytotoxicity with nanomaterials at concentrations of 80 μg/mL compared with 20 and 40 μg/mL was also recorded. It has been confirmed that gallium ions are significantly less toxic than other metallic ions, such as silver, and gallium ions exhibit positive effects on osteoblast differentiation [68]. However, it is still a challenge to optimize the bioavailability of Ga, and it is imperative to reduce the dosage of gallium ions to avoid potential cytotoxicity. Thus, local delivery of Ga is highly recommended, and Ga is preferentially adsorbed on bone tissues due to its affinity to hydroxyapatite (HAP) crystals [24]. Based on the biological performances of various GO/Ga nanocomposites, GO/Ga (1:1) at a concentration of 40 μg/mL exhibited optimal antimicrobial efficacy and cytocompatibility compared with the other nanocomposites as discussed above. Therefore, GO/Ga (1:1) nanocomposites (40 μg/mL) were selected for the subsequent cytological and animal experiments.

3.3. Synergistically enhanced antimicrobial activity of GO/Ga nanocomposites

To further determine whether these novel GO/Ga nanocomposites have synergistically enhanced antibacterial potency, several antibacterial tests, such as the spread plate method, agar disk diffusion method and evaluation of bacterial membrane integrity, were systematically performed and compared as demonstrated in Fig. 2. Bacterial cells with vitality were counted on TSA plates after 4 h of coculture with various of nanomaterials (Fig. 2a and b). Overall, the numbers of live bacteria of the three strains exhibited the following trends: CTRL > GO > GaNPs > GO/Ga ($p < 0.01$); these findings demonstrated that GO/Ga nanocomposites had the most remarkable antibacterial efficacy among these nanomaterials. Meanwhile, the average log-reductions of GO, GaNPs and GO/Ga normalized by CTRL were 0.195-log, 0.618-log and 2.102-log, respectively (Table S4). The GO/Ga nanocomposites displayed significant bactericidal activity against the tested strains with an approximately 2-log reduction in the bacterial counts, indicating that at least 99% of the cocultured bacterial cells were killed by the GO/Ga nanomaterial. Additionally, the antimicrobial efficacy of these nanomaterials was determined by calculating the size of the inhibition zone on TSA plates (Fig. 2c and d). Consistent with the plate counting results, the GaNPs and GO/Ga nanomaterials showed effective inhibition capability on the tested bacterial strains compared to the CTRL and GO ($p < 0.01$). Despite the aforementioned effects of GO nanosheets on bacterial viability, the areas of the inhibition zone of CTRL and GO showed no evident differences among the three strains ($p > 0.05$). Such

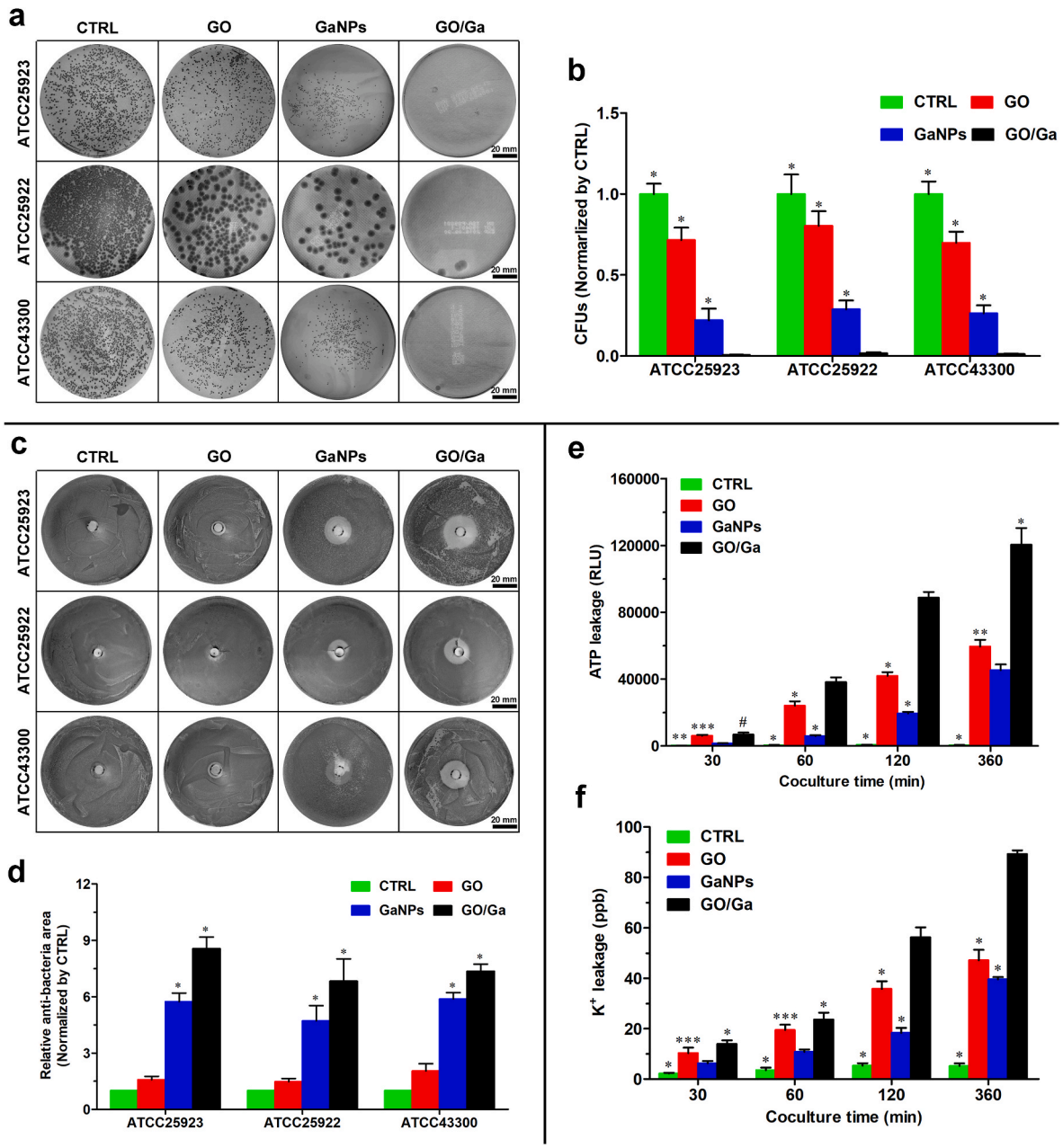

Fig. 2. *In vitro* antimicrobial properties of GO/Ga nanocomposites. (a) Representative images of live colonies of the bacterial cells on TSA plates after 4 h of coculture with different nanomaterials. (b) Quantity of live bacteria confirmed by the spread plate method. (c, d) Determination of the antimicrobial efficacy of nanomaterials on tested strains using the Oxford cup test. (e, f) Observation of bacterial membrane integrity confirmed by the quantity of leakage of ATP and potassium ions (K^+) caused by different nanomaterials during 6 h of coculture. *p < 0.01 compared with the other groups, **p and ***p < 0.05 compared with GaNPs and GO/Ga, respectively, $^{\#}$p < 0.01 compared with CTRL and GaNPs.

a discrepancy could be attributed to the diffusion characteristics of GO nanosheets, and bacterial cells without direct contact with GO nanosheets were not affected. In contrast, GO/Ga nanocomposites have sustained release of Ga^{3+} as described above, leading to a significantly increased inhibition zone compared with other nanomaterials.

Meanwhile, the quantity of released ATP and K^+ was used to evaluate the potential damage to bacterial membrane integrity caused by the GO/Ga nanocomposites (Fig. 2e and f). The concentration of ATP and K^+ collected from the coculture medium increased from 30 min to 360 min, especially GO and GO/Ga. The ATP luminescence intensity and K^+ leakage found in the GO/Ga group were both greater than those in the other groups from 60 min to 360 min ($p < 0.01$), whereas the detected ATP and K^+ in the GaNPs were less than those in the GO group ($p <$ 0.05). Direct physical damage and oxidative stress-associated chemical damage were the two main reasons contributing to the antibacterial actions of the GO nanosheets, which could interact with the phospholipid bilayer and produce oxidation of cellular components [20]. Accompanied by an impaired bacterial membrane, a number of intracellular substances, such as ATP, protein and metallic cations, could be unavoidably released from the cells. As expected, significantly increased ATP and K^+ were observed in the supernatant after the coculture with the GO and GO/Ga nanocomposites, offering direct evidence of damage to the bacterial membrane. More importantly, Ga nanoparticle-induced bacterial membrane damage was also recorded during the 6 h coculture. Previous findings indicate that Ga^{3+} could interfere with ferric iron-dependent metabolic pathways in both gram-positive and

gram-negative bacteria [25]. To obtain a deeper understanding about the synergistic antimicrobial actions and potential mechanism of GO/Ga nanocomposites, morphoplogical changes in tested bacterial strains (*E. coli* and *S.aureus*) resulting from exposure to GO/Ga nanocomposites were evaluated and confirmed by SEM and TEM (Fig. 3). Overall, untreated *E.coli* and *S.aureus* both exhibited normal rod-shaped and round-shaped appearances with relatively intact cell membranes, respectively. However, bacterial cells treated with GaNPs and GO/Ga

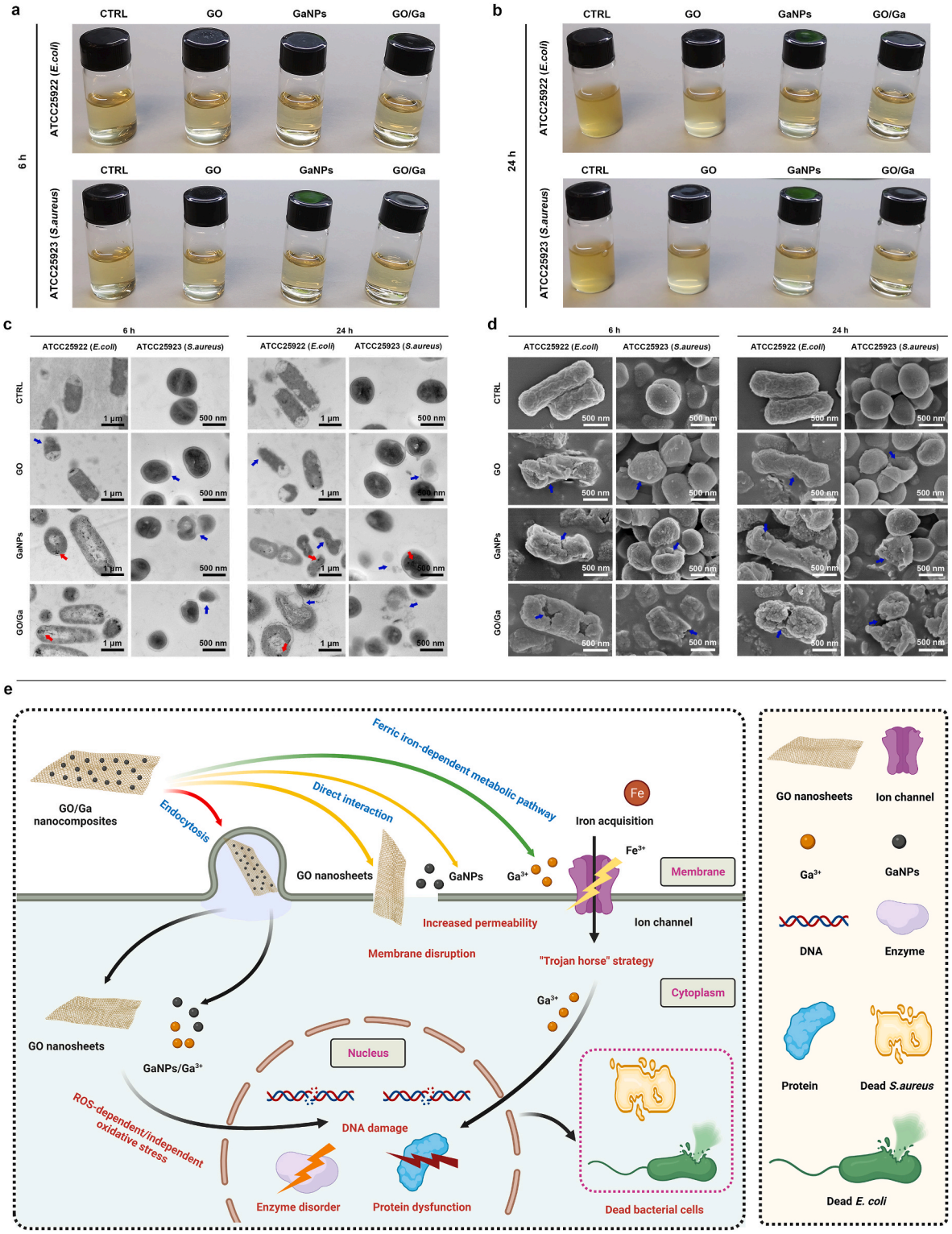

Fig. 3. Morphological analysis of bacteria by microscopy and potential antibacterial mechanisms. (a, b) The appearance of culture medium containing different nanomaterials and tested bacterial strains after 6 and 24 h incubation, respectively. (c) TEM images of *E. coli* and *S. aureus* treated with different nanomaterials. (d) SEM images of *E. coli* and *S. aureus* treated with different nanomaterials. (e) Schematic illustration and summary of potential bacterium inactivation mechanisms via interaction with the GO/Ga nanocomposites according to the results of our study and previous reported findings (Created with BioRender.com). Marked red arrows denote the cellular uptake of released Ga nanoparticles, and blue arrows denote dying or dead cells with destroyed bacterial membrane.

nanomaterials, especially in GO/Ga group, exhibited severely damaged morphological integrity and disrupted membranes, followed by leakage of intracellular contents as also confirmed in Fig. 2e and f. In addition, partially damaged morphologies and integrity of cell walls and membranes were also recorded in GO-treated bacteria. It is noted that the released Ga nanoparticles were found to be closely adhered to the cell walls or inside the tested bacterial strains, signifying a direct interaction between the GO/Ga nanocomposites and the bacterial membranes, which was important to realize the antibacterial potential of GO-based nanomaterials [20]. As demonstrated in the TEM images, intracellular distribution of released Ga nanoparticles were observed in *E. coli*, whereas relatively low GaNPs was found in *S. aureus*, indicating a relatively greater antimicrobial potency of GO/Ga nanocomposites against *E.coli* than *S.aureus*, which is also confirmed in Table S3. The divergent antimicrobial effets of GO/Ga nanocomposites on *E. coli* and *S. aureus* may be caused by different response to the nanomaterials exposure, and degradation of membrane of bacteria further facilitated the penetration of antibacterial components through the barrier into the bacterial interior [18]. In this study, the main forms of gallium released from the GO/Ga nanocomposites were Ga nanoparticles and Ga^{3+} as confirmed by TEM scanning. Besides the particular "Trojan horse" antimicrobial strategy of Ga^{3+} as widely accepted [25,26], as far as we know, this report is the first to offer supporting evidence of the physical or chemical damage to the bacterial membrane caused by Ga nanoparticles. Therefore, our results confirm the hypothesis that both Ga nanoparticles and Ga ions are critical sources that contribute to the antibacterial action of GaNPs-based nanomaterials [36]. Based on the results of our study and previous reported findings [20,25,26,45,71], the possible antibacterial mechanisms of the GO/Ga nanomaterials could be summarized as the following: 1) ROS-dependent or independent oxidative stress; 2) Increased permeability due to bacterial membrane disruption; 3) Competition with Fe^{3+} for incorporation into essential proteins and enzyme due to chemical similarities between Fe^{3+} and Ga^{3+}.

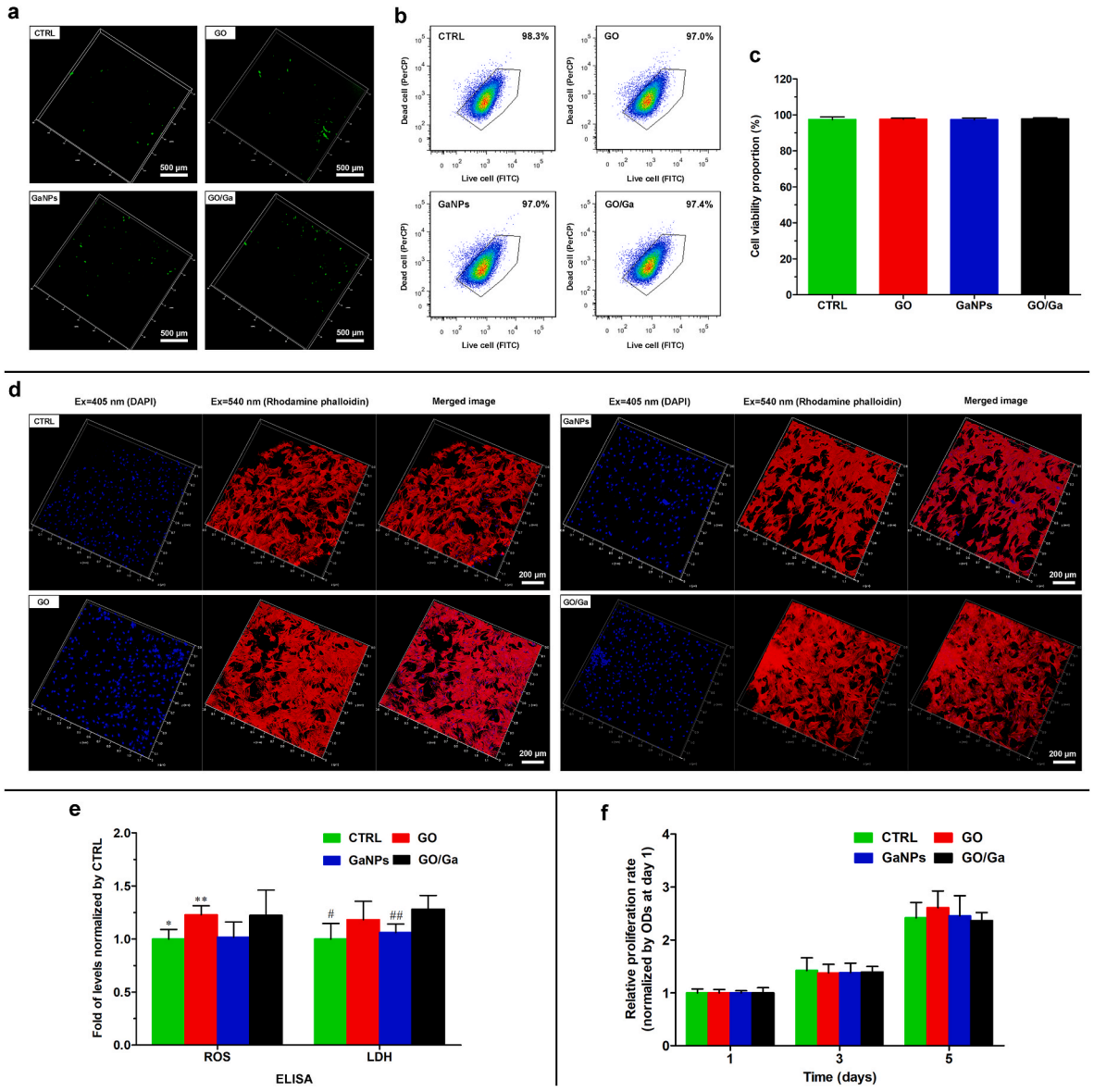

Fig. 4. Investigation of the cytocompatibility of different nanomaterials with rBMSCs. (a) CLSM images of oxidative stress in cells in response to tested nanomaterials after being stained with 2′, 7′-DCFH-DA. (b) Flow cytometry assay of rBMSCs stained with Live/Dead Cell kit, respectively. (c) Quantitative analysis of cell viability using FlowJo software. (d) CLSM observation of rBMSCs stained with DAPI (blue, nuclei) and rhodamine phalloidin fluorescence (red, cytoskeleton). (e) Detection of cellular damage-associated biomarkers (ROS and LDH) using ELISA kits. (f) Quantity of cell proliferation determined by a CCK-8 assay at the indicated time points. *$p < 0.05$ compared with GO and GO/Ga, **$p < 0.05$ compared with GaNPs, $^{\#}p < 0.01$ and $^{\#\#}p < 0.05$ compared with GO/Ga.

3.4. Reduced cytotoxicity of GO/Ga nanocomposites toward osteogenic cells

Considering the equal significance of antimicrobial efficacy and cytocompatibility for GO- based nanomaterials, we subsequently investigated the effects of GO/Ga nanocomposites on the viability and proliferation of rBMSCs. First, rBMSCs demonstrated sparsely distributed green fluorescence in all the groups after being stained with ROS indicator (Fig. 4a), suggesting a slight level of free radical formation in rBMSCs after coculture. The cell apoptosis of rBMSCs after coculture with the nanomaterials was relatively low and there were no significant differences among the four groups ($p > 0.05$) (Fig. 4b and c). Second, a morphological observation of the cytoskeleton of the rBMSCs after coculture with different nanomaterials was performed using CLSM after sequential staining with rhodamine phalloidin and DAPI (Fig. 4d). rBMSCs displayed confluent and clustered morphology with abundant actin filaments and intercellular connections in all the groups, suggesting that the nanomaterials used at the indicated concentration (40 μg/mL) had no obvious adverse effects on the spreading and morphology of the rBMSCs. The initial attachment of bone mesenchymal stem cells over the implants was a pivotal step for the subsequent osseointegration; thus, the GO/Ga nanocomposites could provide an amicable microenvironment for osteoblast differentiation according to their satisfactory cytocompatibility with rBMSCs.

Moreover, two important cellular damage-associated biomarkers, ROS and LDH, were determined by ELISA kits as shown in Fig. 4e. The levels of ROS and LDH observed in the GO and GO/Ga groups were slightly greater than those in the CTRL and GaNPs groups ($p < 0.05$), suggesting that the GO nanosheet had an oxidative stress-related effect on the tested rBMSCs. To further confirm the potential cytotoxicity of GO-based nanomaterials, cell proliferation was recorded and compared after 1, 3 and 5 d of coculture (Fig. 4f). There were no evident differences regarding the proliferative rate of the rBMSCs among these groups within 5 d ($p > 0.05$), indicating that the GO-based nanomaterials exerted no obvious adverse effect on the cell behavior for a relatively longer time. The discrepancy presented in the cytotoxicity of GO/Ga nanocomposites towards bacteria cells and rBMSCs may be caused by different membrane structure, physiological characteristics, size or any other factors, which remains to be further investigated and confirmed. The toxicity and compatibility of GO-based nanoplatforms have been extensively investigated. However, realizing the clinical translation of graphene and its derivatives remains challenging due to potential cytotoxicity at high concentration and extended application [69]. Thus, more dedicated efforts are needed to reduce the cytotoxicity of GO/Ga nanocomposites, and the combination of GO nanosheets and Ga nanoparticles exhibited relatively good cytocompatibility. Considering the aforementioned synergistically enhanced antimicrobial activity and reduced cytotoxicity toward osteogenic cells, GO/Ga nanocomposites could be a feasible and effective therapeutic approach to realize good osseointegration in a bacteria-infected microenvironment.

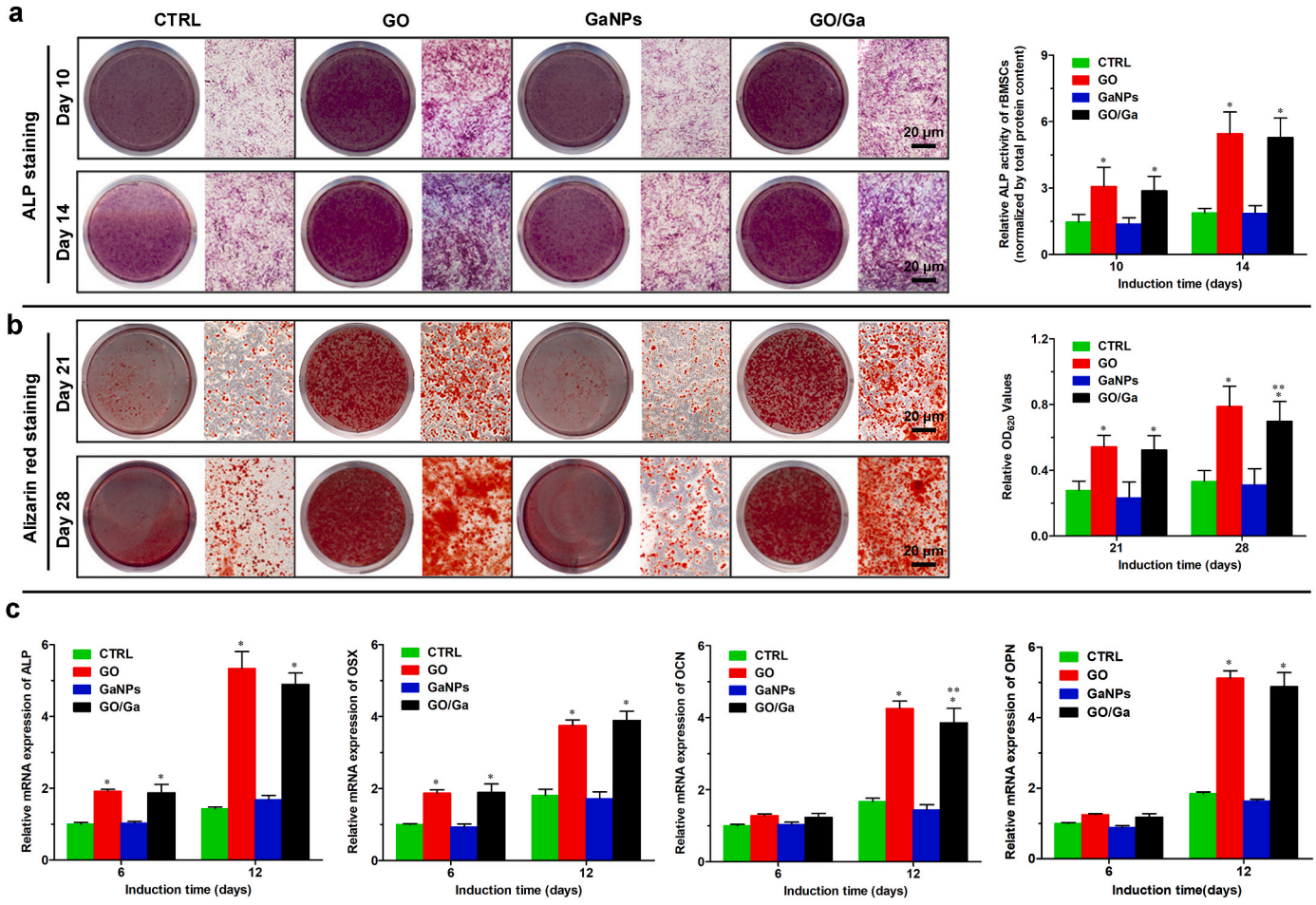

Fig. 5. Osteoblast differentiation of rBMSCs after coculture with different nanomaterials in osteogenic inductive medium. (a) *ALP* staining and quantity of *ALP* activity at 10 and 14 d. (b) Alizarin red staining and quantification of calcium formation at 21 and 28 d. (c) Relative mRNA expression of osteogenic differentiation-related markers (*ALP*, *OSX*, *OCN* and *OPN*) in rBMSCs at 6 and 12 d determined by RT-PCR. These data are the mean levels relative to *GAPDH* and were normalized to the expression levels found in CTRL. *$p < 0.01$ compared with CTRL and GaNPs, **$p < 0.05$ compared with GO.

3.5. Improvement in osteoblastogenesis by GO/Ga nanocomposites

To determine the *in vitro* osteoregenerative potential of GO/Ga nanocomposites, relevant investigations were conducted at the indicated coculture time points. Similarly, the ALP and ARS staining intensities observed in the GO and GO/Ga groups were obviously larger than those in the CTRL and GaNPs groups after 10–28 d of osteogenic induction (Fig. 5a and b), which was confirmed by the corresponding quantitative analysis ($p < 0.01$). In addition, the calcium nodule formation observed in GO/Ga was slightly lower than that in GO ($p < 0.05$), and there were no differences in the osteogenic capability between the CTRL and GaNPs ($p > 0.05$). Furthermore, representative genes, such as *ALP*, *OSX*, *OCN* and *OPN* that are closely related to osteoblast differentiation, were examined after 6 and 12 d of osteogenic induction with the tested nanomaterials (Fig. 5c). As expected, the early markers (*ALP* and *OSX*) were upregulated in the GO and GO/Ga groups compared to those in the CTRL and GaNPs groups at both 6 and 12 d ($p < 0.01$), and the mRNA expression levels of the later markers (*OCN* and *OPN*) were also significantly increased in the GO and GO/Ga groups compared to those in the other two groups at 12 d ($p < 0.01$). No evident differences in the mRNA expression of these genes were recorded between the CTRL and GaNPs groups ($p > 0.05$). The mRNA expression level of *OCN* observed in the GO/Ga group at 12 d was slightly less than that in the GO group ($p < 0.05$), which is in accordance with the ARS staining analyzed above. Our results indicate that both the GO and GO/Ga nanomaterials significantly promoted osteogenic activities compared with the CTRL and GaNPs, and the addition of Ga nanoparticles into the composites demonstrated no evident adverse effects on the osteogenic differentiation of rBMSCs. It has been accepted that derivatives of graphene, such as GO or reduced GO, can facilitate the osteoblast differentiation, rendering them promising candidates for preparing multifunctional nanoengineered bone substitutes [22,66]. Therefore, it is reasonable to build a GO-based platform to combat implant-related bone infection featuring an impaired osteogenic microenvironment between implants and bone tissues. Our results confirm that the osteoregenerative potential of GO/Ga nanocomposites mainly depends on the incorporated GO nanosheets, indicating that the Ga nanoparticles had no visible effects on the osteogenic differentiation of rBMSCs.

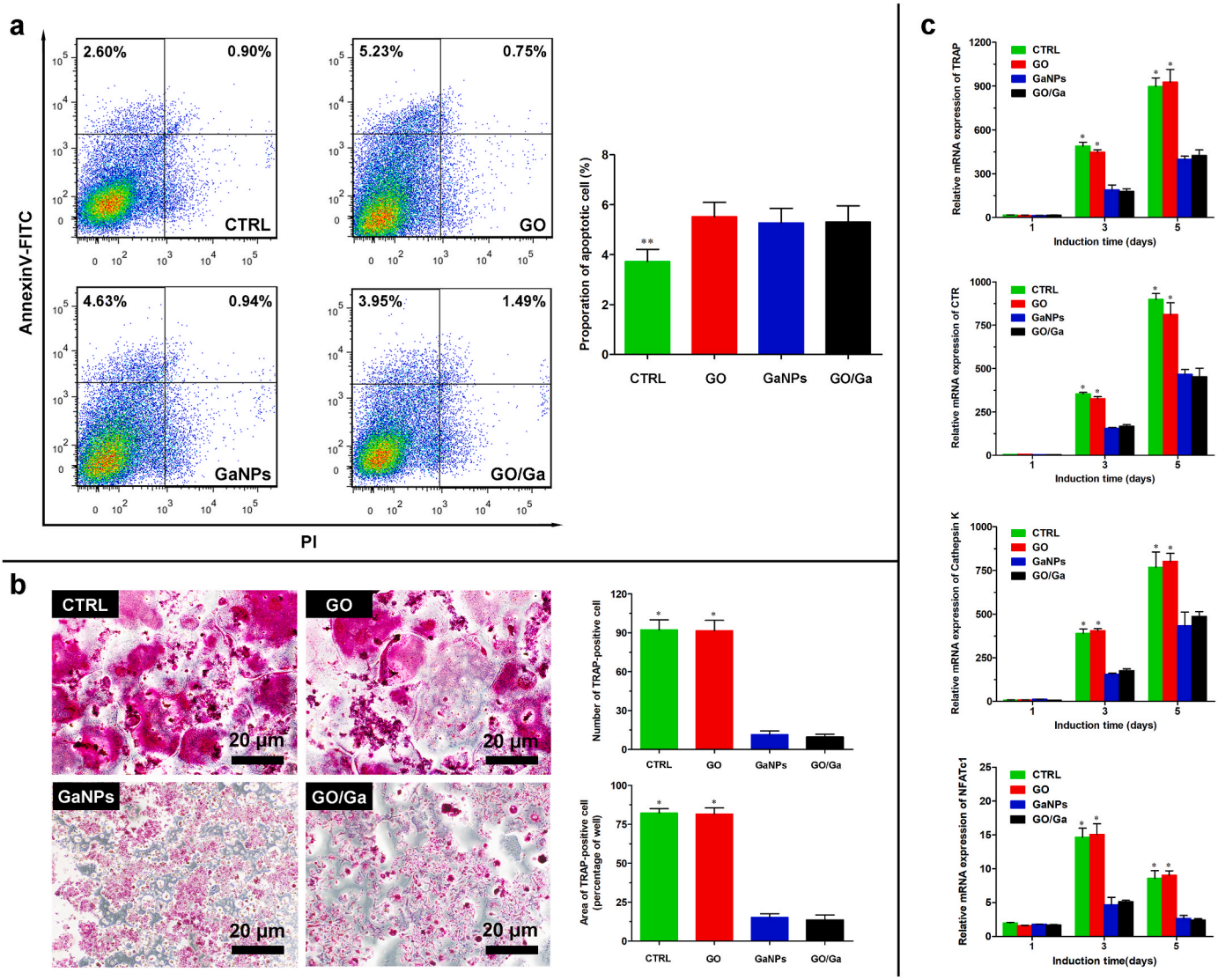

Fig. 6. Osteoclast differentiation of rBMMs after coculture with different nanomaterials in medium supplemented with the indicated concentrations of M-CSF and RANKL. (a) Determination of the apoptotic effect of different nanomaterials on rBMMs using a flow cytometry assay after staining with an Annexin V-FITC Detection kit. (b) Observation of cells after being fixed with 4% PFA and stained with an acid phosphatase staining kit, followed by a quantitative analysis of the area and number of TRAP-positive multinuclear cells. (c) Relative mRNA levels of RANKL-induced expression of osteoclast-specific genes (*TRAP*, *CTR*, *Cathepsin K* and *NFATc1*) in rBMMs at 1, 3 and 5 d determined by RT-PCR. *$p < 0.01$ compared with the GaNPs and GO/Ga groups, **$p < 0.05$ compared with the other groups.

3.6. Suppression of RANKL-induced osteoclastogenesis by GO/Ga nanocomposites

Prior to investigating the regulatory effects of GO/Ga nanocomposites on RANKL-induced osteoclastogenesis, the possible cytotoxicity of the tested nanomaterials was confirmed by Annexin V-FITC staining (Fig. 6a). Although slightly increased cell apoptosis was observed in the GO, GaNPs and GO/Ga groups compared with that in the

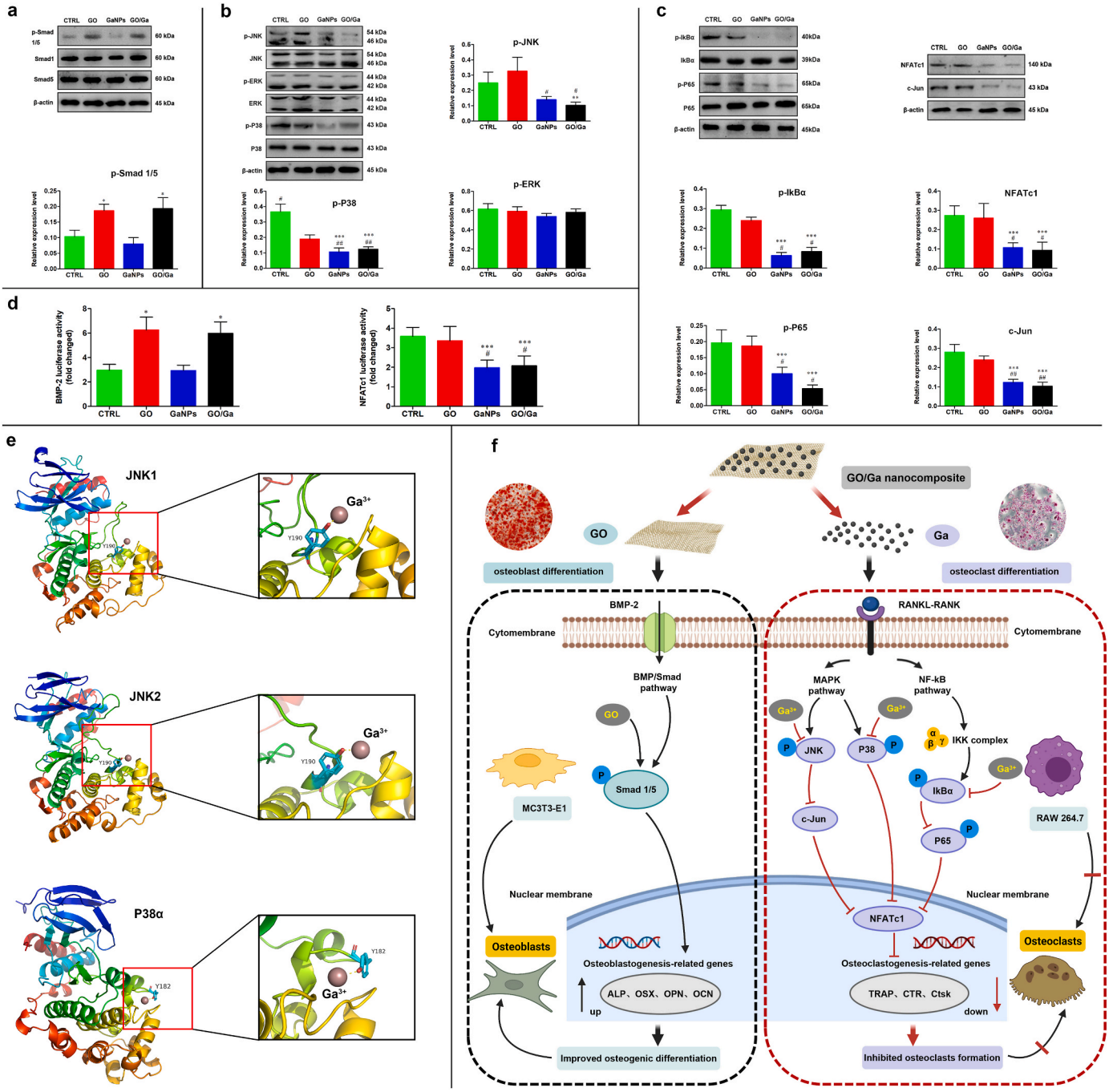

Fig. 7. Investigation of the potential molecular mechanisms of the regulatory effects of GO/Ga nanocomposites on osteoblastogenesis and osteoclastogenesis in MC3T3-E1 and RAW 264.7 cells. (a) Expression features of BMP/SMAD signaling molecules during the osteoblast differentiation of MC3T3-E1 cells after coculture with different nanomaterials for 7 d. (b) Expression features of RANKL-stimulated MAPK signaling molecules during the osteoclast differentiation of RAW 264.7 cells after being pretreated with different nanomaterials for 4 h prior to RANKL (50 ng/mL) stimulation for 30 min. (c) Expression features of RANKL-stimulated NF-κB signaling molecules during the osteoclast differentiation of RAW 264.7 cells after being pretreated with different nanomaterials for 4 h prior to RANKL (50 ng/mL) stimulation for 30 min. The expression levels of NFATc1 and c-Jun were also confirmed after coculture for 3 d with the stimulation of RANKL (50 ng/mL). Overall, the relative expression levels of *p*-Smad 1/5, *p*-JNK, p-P38, *p*-ERK, *p*-IkBα, p-P65, NFATc1 and c-Jun were calculated and normalized by β-actin in terms of the gray band intensities as confirmed by ImageJ software. (d) Luciferase reporter gene assessment of BMP-2 and NFATc1 in MC3T3-E1 and RAW264.7 cells, respectively. Stably transfected cells were treated with different nanomaterials for 6 h with specific stimulation, and the luciferase activities were confirmed by a Pierce™ Gaussia Luminescence Assay kit. (e) Molecular docking of Ga^{3+} with JNK/P38 kinases as demonstrated in binding mode figures using PyMOL visualization software. (f) Schematic diagram of the regulatory mechanisms of GO/Ga nanocomposites involved in osteoblastogenesis and osteoclastogenesis (Created with BioRender.com). *p < 0.01 compared with CTRL and GaNPs, **p < 0.05 and ***p < 0.01 compared with CTRL, #p < 0.01 compared with GO, ##p < 0.05 compared with GO.

CTRL group ($p < 0.05$), the cytotoxic effects of the nanomaterials on osteoclast differentiation could be ignored. Subsequently, the rBMMs in each group were evaluated with TRAP staining (Fig. 6b). Numerous giant multinucleated cells representative of osteoclast differentiation were found in the CTRL and GO groups, whereas an obviously reduced TRAP staining intensity with few positively stained cells was observed in the GaNPs and GO/Ga groups. Moreover, representative markers, such as *TRAP*, *CTR*, *cathepsin K* and *NFATc1* that are closely associated with osteoclast differentiation, were examined by real-time PCR after 1, 3 and 5 d of induction with the tested nanomaterials (Fig. 6c). The quantitative analysis of the mRNA expression of these markers demonstrated that the Ga-containing nanomaterials (GaNPs and GO/Ga) could obviously inhibit relevant gene expression closely related to osteoclast formation compared to the CTRL and GO groups at 3 and 5 d ($p < 0.01$). These findings indicate that only Ga from the prepared nanomaterials contributed to the suppression of osteoclastogenesis, while the GO nanosheets had no evident impacts on osteoclast differentiation. Combined with the osteoblast differentiation results analyzed above, it might be concluded that GO/Ga nanocomposites could serve as effective modulators of osteoblastogenesis and osteoclastogenesis due to the GO nanosheets and released Ga ions, respectively. As a potential anti-osteoporotic agent used in the treatment of Paget's diseases [23,24], the semimetallic element gallium (Ga) displayed a dose-dependent inhibitory effect on *in vitro* osteoclastic resorption without negatively affecting osteoblast function [27], which is also confirmed in the present study. Meanwhile, Ga-containing bioceramics or scaffolds are considered effective substitutes for reconstructing bone defects in osteoporotic environments [29,70]. In addition, the reduction of osteocalst activity could facilitate the deposition of calcium and phosphorus in bone tissue, leading to enhanced stablility of bone with more HA crystals that exhibits greater resistance to bone resorption caused by bacterial infection in this study [24,71]. Therefore, the osteogenic activity of GO/Ga nanocomposites depends on the destructive effect of gallium on osteoclatsogenesis and promotive effect of GO on osteoblastogenesis. The synthesis and application of Ga-sustained release biomaterials is of great clinical importance; however, these investigations only focused on the direct influences of Ga^{3+} on osteoclast activities. In this research, for the first time, the potent effects of released GaNPs/Ga^{3+} from the surface of GO nanosheets on restraining osteoclast activities were confirmed, suggesting that nanostate gallium may contribute to the regulation of osteoclastic performances. In summary, our study offers novel and valuable insight into the direct interactions between gallium nanoparticles and bacteria and osteoclasts, broadening the potential utilization of gallium-based materials for the improvement of anti-infective and anti-resorptive actions.

3.7. Molecular mechanisms of the regulatory effects of GO/Ga nanocomposites on osteoblastogenesis and osteoclastogenesis

Based on the regulatory effects of GO/Ga nanocomposites on osteoblastogenesis and osteoclastogenesis described above, western blotting, luciferase reporter gene activity and molecular docking analysis were performed to further confirm the potential molecular mechanisms underlying these regulatory actions (Fig. 7). As demonstrated in Fig. 7a, the Smad 1/5 phosphorylation level was obviously upregulated in the GO and GO/Ga groups compared to that in the other two groups, indicating that the BMP/Smad signaling pathway was involved in the modulatory actions of the GO-containing nanomaterials toward osteoblast differentiation, which is consistent with the previously reported "nanoreservoir" mechanism of the osteogenesis-enhancing activity of GO-based nanosheets on hBMSCs [22]. Then, the effects of Ga-containing nanomaterials on RANKL-induced MAPK and NF-κB coactivation during osteoclast formation were explored. It found that the phosphorylation of ERK was steady with no significant differences among the four groups after the RANKL stimulation, whereas the phosphorylation of JNK and P38 was evidently attenuated after the administration of GaNPs and GO/Ga, suggesting that Ga could inhibit RANKL-stimulated MAPK activation by targeting the phosphorylation of JNK and P38 without affecting the phosphorylation of ERK (Fig. 7b). It was found that the constitutive activation of MAPK was closely related to the upregulation of NF-κB phosphorylation, indicating potential crosstalk between the MAPK and NF-κB pathways [53]. In this study, the expression of phosphorylated IkBα and P65 was significantly attenuated in the osteoclasts treated with GaNPs and GO/Ga, followed by the inhibition of IkBα degradation and inactivation of the NF-κB pathways (Fig. 7c). Subsequently, the variation in downstream molecules, such as c-Jun and NFATc1, originating from the MAPK and NF-κB pathways, respectively, were explored and confirmed. It found that the expression levels of c-Jun and NFATc1 were both inhibited, signifying that Ga could target both the upstream and downstream of MAPK and NF-κB pathways to impact osteoclast differentiation. In addition, a luciferase reporter gene assessment of BMP-2 and NFATc1 in MC3T3-E1 and RAW264.7 cells, respectively, was employed to verify these findings in a western blot assay (Fig. 7d). As expected, the activities of BMP-2 and NFATc1 in the tested cells were significantly reduced after the administration of Ga-containing nanomaterials.

To further explore the role of BMP/Smad, MAPK and NF-κB signaling in the biological effects of GO/Ga nanocomposites on osteoblastogenesis and osteoclastogenesis as analyzed in Figs. 5 and 6, a siRNA-mediated BMP-2 knockdown and specific activators of JNK, P38 and NF-κB with indicated concentration were used to perform relevant reverse validation experiments as previously confirmed [53–56] (Fig. S2). As expected, the protein levels of *p*-Smad 1/5 and BMP-2 were both significantly reduced in siRNA-treated groups than in the corresponding vehicle controls. It was confirmed that the addition of activators of JNK, P38 and NF-κB could visibly promote the expression levels of *p*-IkBα and p-P65, *p*-JNK and p-P38, contributing to the increased protein expression of downstream molecules (c-Jun and NFATc1) originated from the MAPK and NF-κB pathways. Our results indicated that the activation of the BMP/Smad signaling induced by GO-incorporated nanomaterials (GO and GO/Ga) was blocked after the administration of BMP-2- specific siRNA duplexes, and addition of agonist of MAPK (Anisomycin and Asiatic acid) and NF-κB (Betulinic acid) reversed the inhibitory effects of Ga-containing nanomaterials (GaNPs and GO/Ga) on MAPK and NF-κB pathways as demonstrated in Fig. 7, signifying that GO/Ga nanocomposites exhibited osteogenic potential and inhibitory effects on osteoclast differentiation by regulating the BMP/Smad, MAPK and NF-κB signaling pathways.

Eventually, the binding affinity of Ga^{3+} toward certain amino acids in relevant proteins (JNK-1, JNK-2 and P38α) was confirmed by a computational molecular docking analysis (Fig. S3). The results of the gallium ion docking these three targets demonstrated that the corresponding ligand could be embedded into the binding pockets of JNK1, JNK2 and P38a by establishing molecular bonds with tyrosine 190, 190 and 182, respectively (Fig. 7e). The molecular docking results indicate that GaNPs and GO/Ga nanomaterials could suppress RANKL-induced MAPK activation by targeting JNK/p38 kinases, leading to significantly decreased osteoclast formation. As previously confirmed, the suppression of the MAPK and NF-κB pathways could reactivate BMP/Smad signaling, contributing to the upregulated expression of osteoblastogenesis-associated genes [53]. In this study, activated BMP/Smad signaling and inhibited MAPK/NF-κB signaling were observed during the regulation of osteogenic differentiation and osteoclast formation. Our results indicate possible crosstalk among the BMP/Smad, MAPK and NF-κB signaling pathways, which remains to be further investigated in an osteogenic cell and osteoclast coculture system. In particular, NF-κB signaling played a pivotal role in the early innate immune response to *S. aureus* infection-induced osteomyelitis, and blocking NF-κB signaling could reduce the expression of relevant inflammatory cytokines that facilitate the development of bacterial infection in bone tissues [33]. In another study, constitutively activated P38/MAPK and Smad signaling caused by CHI3L1 aggravated bone

erosion in a *S. aureus*-infected osteomyelitis model in a murine model [34]. More importantly, the host immune responses were regarded as major drivers of pathologic bone remodeling during osteomyelitis, and several proinflammatory factors, such as IL-1α, IL-6, IL-17 and TNF-α, were found in *S. aureus* infection-related bone destruction, which, in turn, inevitably promoted RANKL-induced osteoclast differentiation [35]. Considering the biological effects of GO/Ga nanocomposites on bacteria, osteogenic cells and osteoclasts as previously stated along with the specific pathogenesis of osteomyelitis, it is expected that this novel GO/Ga nanoderivative could attenuate bacterial infection-triggered osteolysis and promote osseointegration by modulating the BMP/Smad, MAPK and NF-κB signaling pathways (Fig. 7f), which remains to be further validated in an implant-related infection model in rats as discussed later.

3.8. Reduced osteolysis and better osseointegration caused by GO/Ga nanocomposites in an implant-related infection model in rats

According to previously reported animal models with some modifications [59,60], we clarified the *in vivo* therapeutic efficacy of GO/Ga nanocomposites in an aggressive osteolysis microenvironment based on an implant-associated infection model in SD rats (Fig. 8a). As shown in Fig. 8b, typical signs of implant-associated bone infection, including osteolysis, implant loosening and condyles destruction, were observed in Group I on the day of sacrifice at 5 w, whereas these signs of progressive bone infection were obviously alleviated in Group IGG. These radiographic manifestations were further confirmed by a relevant morphometric analysis as shown in Fig. 8c and d. The quantitative evaluation of longitudinal and transverse sections from the region of interest from the harvested femoral shafts and condyles indicated that the BV/TV, BMD and Tb. Th of Group I were evidently reduced compared to those of the other three groups ($p < 0.05$), and Group I also exhibited higher surface porosity and Tb. Sp, which is representative of osteolysis, compared to the other groups ($p < 0.01$). Additionally, no obvious signs of impaired integrity were found in Groups U and UGG, indicating that the administration of GO/Ga nanocomposites had no adverse effects on bone morphology. In contrast, evidently improved osseointegration between the implants and bone tissues was recorded in Group UGG, indicating that the GO/Ga nanocomposites facilitated *in vivo* osteoblast differentiation and new bone deposition.

In addition to the radiographic assessment, a series of histological analyses were performed to verify the results of the micro-CT reconstructed images (Fig. 9a). Consistent with the radiological manifestations, typical signs of bone infection, such as osteonecrosis, fibrosis and abscesses, were observed in Group I, and these morphological changes were evidently mitigated in Group UGG. Moreover, there was no obvious histopathological destruction in the collected femoral bone from Groups U and IGG (Fig. 9b and c). A number of TRAP-positive osteoclasts were found in the bone slices from Group U, with evidently reduced osteoclasts observed in the other groups. It has been confirmed that GO/Ga nanocomposites could restrain osteoclast formation by regulating the crosstalk between the MAPK and NF-κB signaling pathways, which contributed to the improvement in osteolysis caused by bacterial infection in animal models. The number of residual bacteria shown in the Giemsa-stained sections from Groups U, IGG and UGG was notably less than that in the sections from Group I, suggesting that biofilms formed on the implants or bone tissues were effectively eradicated after the application of GO/Ga nanocomposites. Excessive osteoclast formation and inflammatory reactions are regarded as the major reasons for bone resorption and osteolysis, and the effectiveness of antibacterial potency is closely related to the outcomes of bone destruction [15,72]; thus, GO/Ga nanocomposites with anti-infective and anti-resorptive activities could substantially restrain the progress of implant-associated bone infection. In accordance with a modified histopathological scoring criterion [63], a quantitative evaluation of the manifestations of bone infection in slices obtained from the four groups was conducted and compared. As expected, the histopathological scores of the longitudinal and transverse sections obtained from Groups I and IGG were greater than those in slices from Groups U and UGG ($p < 0.01$), followed by a reduction in group IGG compared with that in Group I ($p < 0.05$) (Fig. 9e, g). Moreover, fluorescent calcein staining and SB-VG staining were employed to record the newly formed bone tissues around the bone-implant interfaces in nondecalcified slices. Significantly improved osseointegration was observed in the slices from Groups U, IGG and UGG, and poor osseointegration with obvious implant loosening was found in the sections from Group I. These findings were further verified by the quantification of the BIC values (Fig. 9d, f). The BIC value of the sections from Group I was less than that of the sections from the other groups ($p < 0.01$), and the sections from Group UGG exhibited the highest BIC value among the four groups ($p < 0.01$). Taken together, the radiographic and histopathological evaluation of the animal model provided credible evidence supporting the effective therapeutic outcomes after the administration of GO/Ga nanocomposites in both aseptic and bacterial infected environments.

More importantly, the *in vivo* biosafety of the GO/Ga nanocomposites was determined according to previously reported protocols using metal-incorporated biomaterials [21,64,73]. The organizational structures of the heart, lung, spleen, liver and kidney evaluated by H&E staining in Groups U, IGG and UGG exhibited no obvious pathological changes, except for some congestive changes observed in the organs from Group I, which may have been caused by local bacterial infection (Fig. 10a). The results of the routine blood examination indicated that the number of WBCs and percentage of neutrophils of the bacterial-infected animals without treatment with the GO/Ga nanocomposites (Group I) were evidently greater than those in the other three groups ($p < 0.01$), whereas these values in Groups U, IGG and UGG were within the normal range. Similarly, slightly impaired hepatic and renal function was found in the animals in Group I compared to those in the other groups ($p < 0.05$) (Fig. 10b). In addition, the Ga^{3+} deposition in major organs was confirmed by an ICP-OES analysis (Fig. S4). No evident difference was recorded between Groups IGG and UGG, and the Ga^{3+} concentration in these organs was much lower than the level that could generate detrimental impacts on general metabolic functions as previously confirmed [23,24]. Notably, the biocompatibility, biodistribution and biodegradability of graphene-based nanomaterials as novel biomaterial for regenerative medicine applications deserve special attention [74]. It has been reported that dextran-functionalized GO nanosheets could be cleared from the experimental mice without any visible toxicity after one week of intravenous injection [75]. Consistent with the previous finding, non-observed residue or accumulation of GO was found in histological sections of bone and major organs from the rats in the present study after three weeks of intramedullary injection of GO-based nanomaterials. Thus, our results provide critical information regarding the biodegradability and biocompatibility of GO/Ga nanocomposites as a potential candidate for the manufacturing of bone repair implants in future clinical scenarios. Additionally, the *in vivo* pharmacokinetics and long-term biosafety of these nanomaterials remain to be systematically investigated, and it is anticipated that the on-going development and optimization of relevant therapeutic strategies could accelerate the promising applications in tissue engineering.

4. Conclusions

In the current study, GO/Ga nanoderivatives were successfully synthesized via modified low- temperature ultrasonic emulsification and *in situ* deposition. The effectiveness of the GO/Ga nanocomposites was confirmed by a series of *in vitro* experiments, indicating that this novel nanoplatform had well-marked antibacterial activity, osteoregenerative capability and an inhibitory effect on osteoclastogenesis. Our preliminary investigation of the latent molecular mechanisms of the regulation of osteoblast and osteoclast differentiation caused by the GO/Ga nanocomposites suggested potential crosstalk among the BMP/Smad,

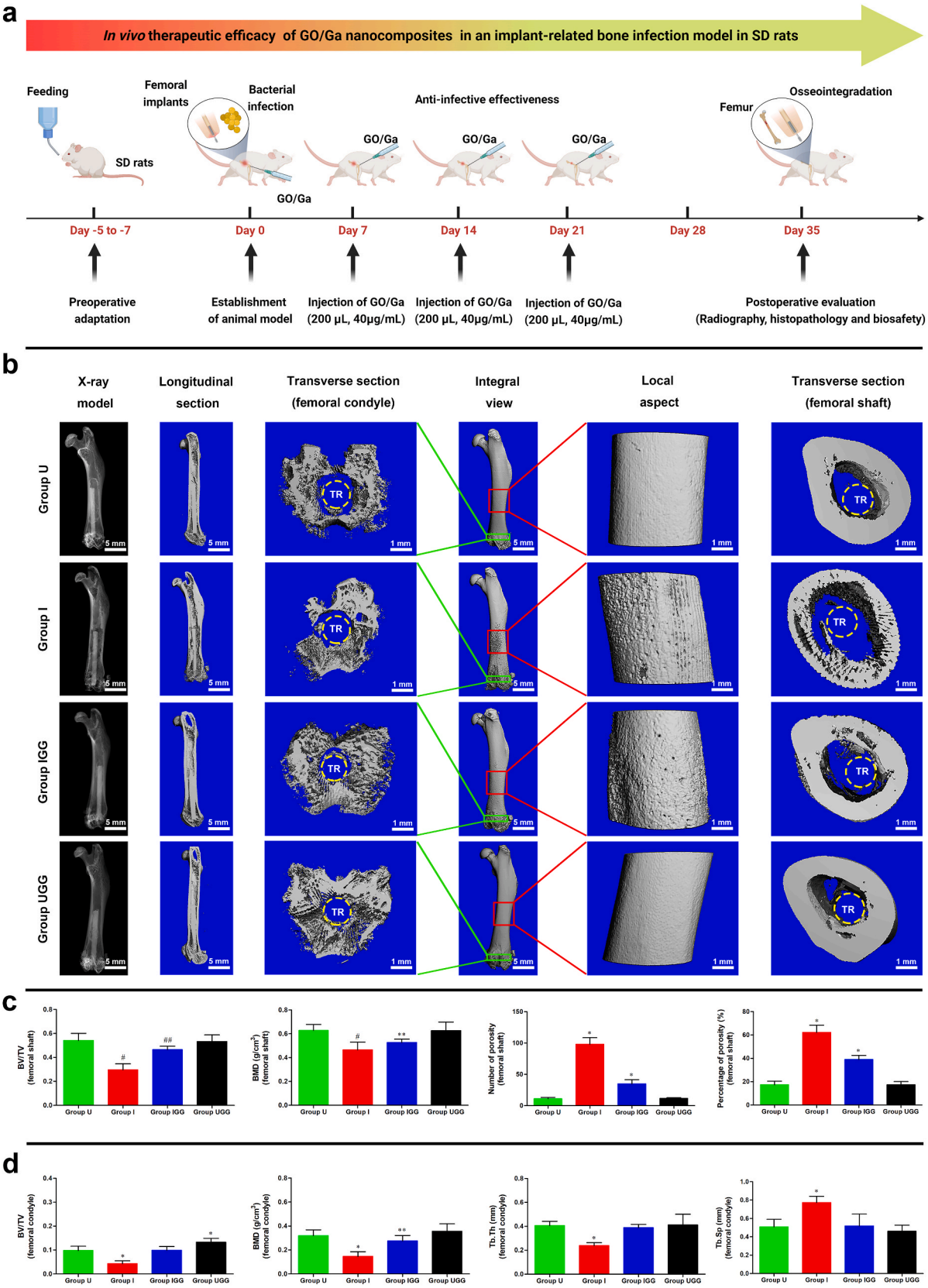

Fig. 8. Investigation of the *in vivo* therapeutic efficacy of GO/Ga nanocomposites on implant-related bone infection. (a) Schematic description of the *in vivo* experimental procedures in SD rats (Created with BioRender.com). (b) Systematic evaluation of a microCT-based radiographic analysis of infection-associated osteolysis and bone-implant integration. (c) Morphometric data (BV/TV, BMD and cortical bone porosity) of reconstructed sections in selected ROIs (red rectangle) from harvested femoral shafts. (d) Morphometric data (BV/TV, BMD, Tb. Th and Tb. Sp) of reconstructed sections in selected ROIs (green rectangle) from harvested femoral condyles. Yellow dotted circles represent implants. TR, titanium rods. *$p < 0.01$ and $^{\#\#}p < 0.05$ compared with the other groups, **$p < 0.05$ compared with Group UGG, $^{\#}p < 0.05$ compared with Groups U and UGG.

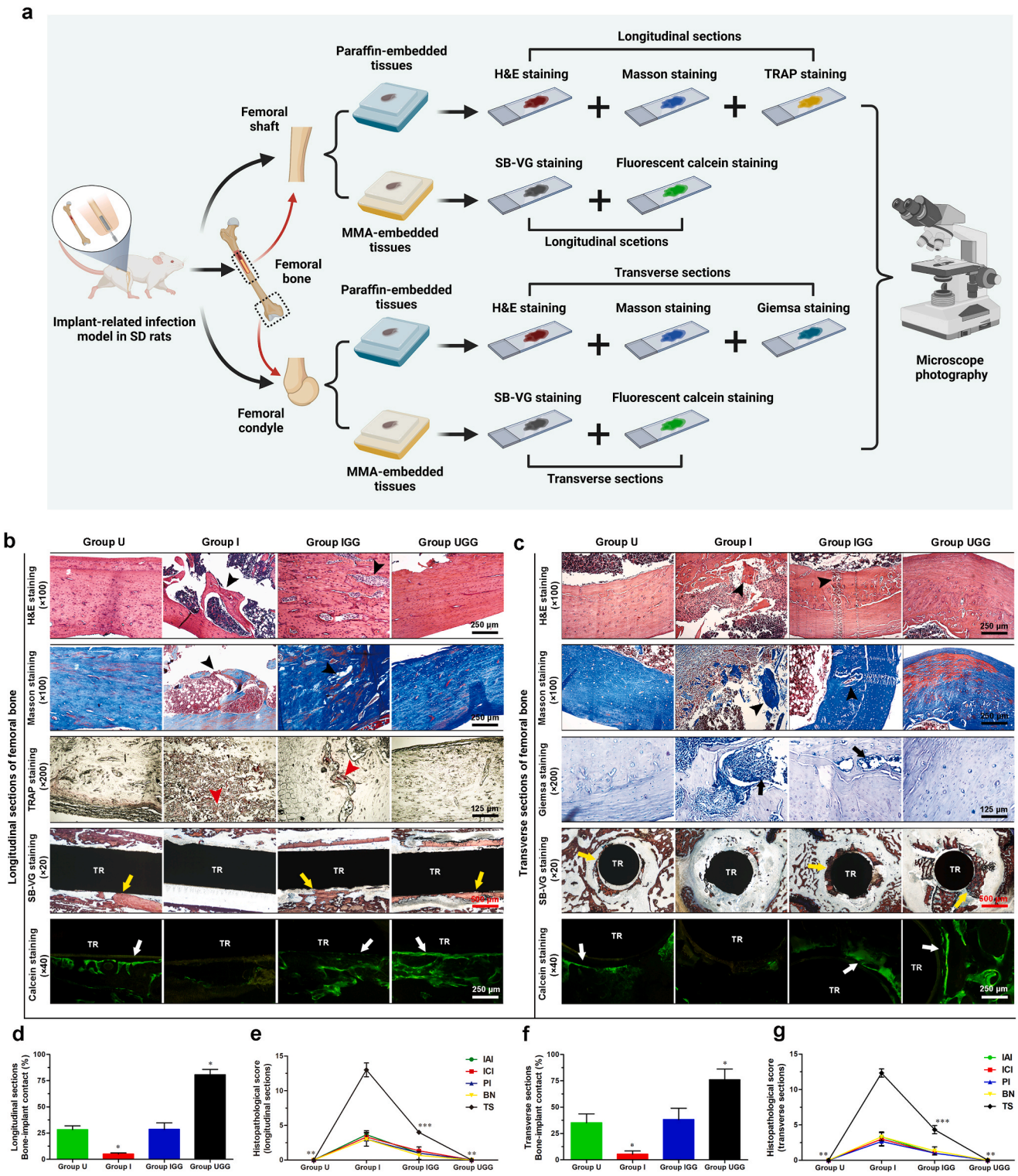

Fig. 9. Histopathological analysis of bacterial-associated osteolysis and bone integration in an implant-related infection model in rats. (a) Schematic illustration of preparation and staining of the histopathological sections (Created with BioRender.com). (b) Representative images of longitudinal sections of femoral bone. (c) Representative images of transverse sections of femoral bone. (d, e) Quantity of bone-implant contact (BIC) and histopathological scores of longitudinal sections. (f, g) Quantity of BIC and histopathological scores of transverse sections. For the decalcified sections, hematoxylin eosin (H&E) and Masson's trichrome staining were utilized to confirm the bone morphology, TRAP staining was utilized to observe the active osteoclasts, and Giemsa staining was used to confirm the bacterial burden. For the nondecalcified sections, combined Stevenel's blue and Van Gieson (SB-VG) staining was used to evaluate bone integration at the bone-implant interface. Fluorescent calcein staining was used to trace newly formed bone tissues around the implants. The black arrowheads represent osteolysis or cortical bone destruction, the red arrowheads represent TRAP-positive osteoblasts, the black arrows indicate residual bacteria, and the yellow and white arrows indicate newly formed bone tissues around the implants. TR, titanium rods. *$p < 0.01$ compared with the other groups, **$p < 0.01$ compared with Groups I and IGG, ***$p < 0.05$ compared with Group I.

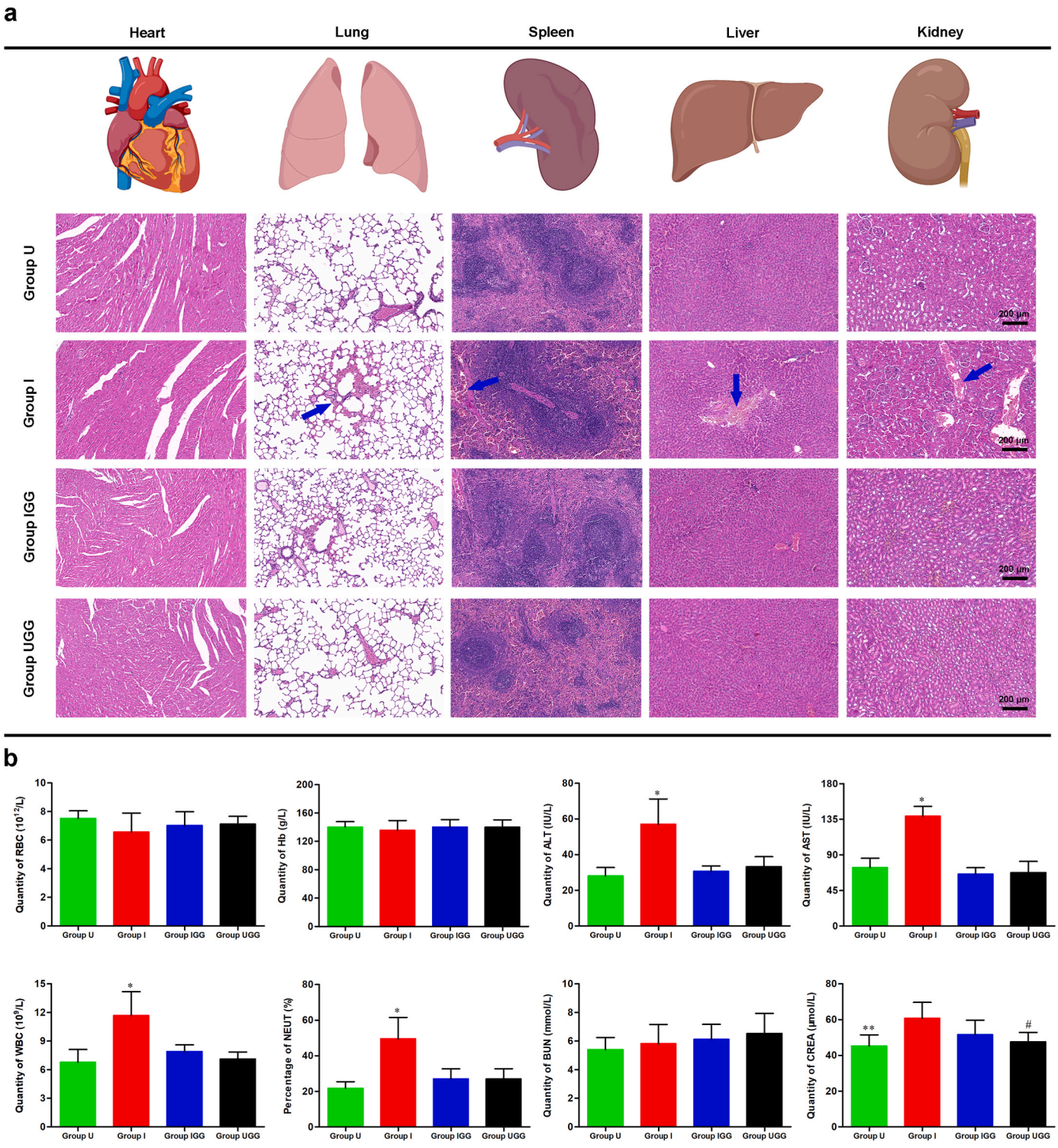

Fig. 10. Determination of the *in vivo* biosafety of GO/Ga nanocomposites. (a) Representative H&E staining images of vital organs (heart, lung, spleen, liver and kidney) in each group (Created with BioRender.com). (b) Laboratorial confirmation of a routine blood examination and blood biochemical tests of rats at the time of sacrifice. Blue arrows represent local congestive lesions caused by bacterial infection-associated inflammatory responses in major organs. *$p < 0.01$ compared with the other groups, **$p < 0.01$ and $^{\#}p < 0.05$ compared with Group I.

MAPK and NF-κB signaling pathways. Furthermore, an *in vivo* infectious microenvironment in a rat model of implant-related femoral osteomyelitis was established, and our results demonstrate that osteolysis and implant loosening with good biocompatibility were alleviated in the animals treated with GO/Ga nanocomposites. Moreover, the administration of GO/Ga nanocomposites significantly facilitated new bone formation located in implant-bone interfaces. Considering the antimicrobial, antiresorptive and osteoconductive properties of GO/Ga nanocomposites, there is a reasonable prospect that these GaNPs-decorated GO nanosheets have great potential for fabricating multifunctional implants to prevent bacteria-induced osteomyelitis in plastic or orthopedic surgery.

CRediT authorship contribution statement

Ying Yang: Conceptualization, Data curation, Formal analysis, Funding acquisition, Project administration, Validation, Investigation, Writing – original draft, Writing – review & editing. **Min Li:** Formal analysis, Methodology, Investigation, Validation, Writing – original draft. **Bixia Zhou:** Formal analysis, Validation, Investigation. **Xulei Jiang:** Formal analysis, Validation, Investigation. **Dou Zhang:** Conceptualization, Validation, Resources, Writing – review & editing. **Hang Luo:** Funding acquisition, Project administration, Validation, Resources, Writing – review & editing.

Declaration of competing interest

The authors declare that they have no known competing financial interests or personal relationships that could have appeared to influence the work reported in this paper.

Acknowledgements

Our study was financially supported by the National Natural Science Fundation for Youth of China (Nos. 81802136), the Natural Science Fundation for Youth of Hunan Province (Nos. 2020JJ5939), the Post-doctoral Science Fundation of China (Nos. 2018M643005), the National Natural Science Fundation of China (Nos. 52172265), and the Science Fundation for Youth of Xiangya Hospital, Central South University (Nos. 2017Q18). Additionally, we want to acknowledge Mr. Xiaobin Zhou and Yecheng Fan from Shiyanjia Lab (www.shiyanjia.com) for providing assistance to the materials characterizations in this study. We deeply appreciate the valuable suggestion and kindly assistance from Prof. Changjun Li (Department of Endocrinology, Xiangya Hospital, Central South University) during the revision of this work.

Appendix A. Supplementary data

Supplementary data to this article can be found online at https://doi.org/10.1016/j.bioactmat.2022.07.015.

References

[1] A. Ghimire, J. Song, Anti-periprosthetic infection strategies: from implant surface topographical engineering to smart drug-releasing coatings, ACS Appl. Mater. Interfaces 13 (18) (2021) 20921–20937.
[2] K. Chae, W.Y. Jang, K. Park, J. Lee, H. Kim, K. Lee, C.K. Lee, Y.S.H. Lee, J. Seo, Antibacterial infection and immune-evasive coating for orthopedic implants, Sci. Adv. 6 (44) (2020), eabb0025.
[3] B.F. Ricciardi, G. Muthukrishnan, E.A. Masters, N. Kaplan, J.L. Daiss, E. M. Schwarz, New developments and future challenges in prevention, diagnosis, and treatment of prosthetic joint infection, J. Orthop. Res. 38 (7) (2020) 1423–1435.
[4] M. Zaborowska, F. Vazirisani, F.A. Shah, R. Firdaus, O. Omar, K. Ekström, M. Trobos, P. Thomsen, Immunomodulatory effects exerted by extracellular vesicles from *Staphylococcus epidermidis* and *Staphylococcus aureus* isolated from bone-anchored prostheses, Biomaterials 278 (2021), 121158.
[5] M.I. Hofstee, G. Muthukrishnan, G.J. Atkins, M. Riool, K. Thompson, M. Morgenstern, M.J. Stoddart, R.G. Richards, S.A.J. Zaat, T.F. Moriarty, Current concepts of osteomyelitis: from pathologic mechanisms to advanced research methods, Am. J. Pathol. 190 (6) (2020) 1151–1163.
[6] L.H. Cobb, E.M. McCabe, L.B. Priddy, Therapeutics and delivery vehicles for local treatment of osteomyelitis, J. Orthop. Res. 38 (10) (2020) 2091–2103.
[7] R.O. Darouiche, Treatment of infections associated with surgical implants, N. Engl. J. Med. 350 (14) (2004) 1422–1429.
[8] B. Parsons, E. Strauss, Surgical management of chronic osteomyelitis, Am. J. Surg. 188 (2004) 57–66.
[9] R.K. Wassif, M. Elkayal, R.N. Shamma, S.A. Elkheshen, Recent advances in the local antibiotics delivery systems for management of osteomyelitis, Drug Deliv. 28 (1) (2021) 2392–2414.
[10] H. Liu, Y.L. Tang, S.Y. Zhang, H. Liu, Z.J. Wang, Y. Li, X.L. Wang, L. Ren, K. Yang, L. Qin, Anti-infection mechanism of a novel dental implant made of titanium-copper (TiCu) alloy and its mechanism associated with oral microbiology, Bioact. Mater. 8 (2021) 381–395.
[11] M.Y. Zhu, J. Fang, Y.L. Li, C.X. Zhong, S.H. Feng, X. Ge, H.X. Ye, X.F. Wang, W. W. Zhu, X. Lu, F.Z. Ren, The synergy of topographical micropatterning and Ta-TaCu bilayered thin film on titanium implants enables dual-functions of enhanced osteogenesis and anti-infection, Adv. Healthc. Mater. 10 (9) (2021), e2002020.
[12] Y.F. Zhuang, L. Ren, S.Y. Zhang, X. Wei, K. Yang, K.R. Dai, Antibacterial effect of a copper-containing titanium alloy against implant-associated infection induced by methicillin- resistant *Staphylococcus aureus*, Acta Biomater. 119 (2021) 472–484.
[13] D. Chopra, K. Gulati, S. Ivanovski, Understanding and optimizing the antibacterial functions of anodized nano-engineered titanium implants, Acta Biomater. 127 (2021) 80–101.
[14] K. Xie, Z. Zhou, Y. Guo, L. Wang, G.Y. Li, S. Zhao, X.M. Liu, J. Li, W.B. Jiang, S. L. Wu, Y.Q. Hao, Long-term prevention of bacterial infection and enhanced osteoinductivity of a hybrid coating with selective silver toxicity, Adv. Healthc. Mater. 8 (5) (2019), e1801465.
[15] Y. Yang, L.Y. Chu, S.B. Yang, H.B. Zhang, L. Qin, O. Guillaume, D. Eglin, R. G. Richards, T.T. Tang, Dual-functional 3D-printed composite scaffold for inhibiting bacterial infection and promoting bone regeneration in infected bone defect models, Acta Biomater. 79 (2018) 265–275.
[16] T. Lin, Y. Tamaki, J. Pajarinen, H.A. Waters, D.K. Woo, Z.Y. Yao, S.B. Goodman, Chronic inflammation in biomaterial-induced periprosthetic osteolysis: NF-κB as a therapeutic target, Acta Biomater. 10 (1) (2014) 1–10.
[17] S. Chen, S. Zhang, Y.F. Wang, X. Yang, H. Yang, C.Y. Cui, Anti-EpCAM functionalized graphene oxide vector for tumor targeted siRNA delivery and cancer therapy, Asian J. Pharm. Sci. 16 (5) (2021) 598–611.
[18] C. Hu, Y.J. Yang, Y.Q. Lin, L.L. Wang, R.Y. Ma, Y.L. Zhang, X.L. Feng, J.R. Wu, L. L. Chen, L.Q. Shao, GO-based antibacterial composites: application and design strategies, Adv. Drug Deliv. Rev. 178 (2021), 113967.
[19] Z.J. Zhang, Y.K. Wang, W.S.Y. Teng, X.Z. Zhou, Y.X. Ye, H. Zhou, H.X. Sun, F. Q. Wang, A. Liu, P. Liu, W.G. Cui, X.H. Yu, Y. Wu, Z.M. Ye, An orthobiologics-free strategy for synergistic photocatalytic antibacterial and osseointegration, Biomaterials 274 (2021), 120853.
[20] M.D. Rojas-Andrade, G. Chata, D. Rouholiman, J.L. Liu, C. Saltikov, S.W. Chen, Antibacterial mechanisms of graphene-based composite nanomaterials, Nanoscale 9 (2017) 994–1006.
[21] Y. Yang, Z.G. Dong, M. Li, L.H. Liu, H. Luo, P. Wang, D. Zhang, X.H. Yang, K. C. Zhou, S.R. Lei, Graphene oxide/copper nanoderivatives-modified chitosan/hyaluronic acid dressings for facilitating wound healing in infected full-thickness skin defects, Int. J. Nanomed. 15 (2020) 8231–8247.
[22] Z. Li, S.Q. Xiang, Z.X. Lin, E.N. Li, H. Yagi, G.R. Cao, L. Yocum, L. Li, T.J. Hao, K. K. Bruce, M.R. Fritch, H.L. Hu, B. Wang, P.G. Alexander, K.A. Khor, R.S. Tuan, H. Lin, Graphene oxide-functionalized nanocomposites promote osteogenesis of human mesenchymal stem cells via enhancement of BMP-SMAD1/5 signaling pathway, Biomaterials 277 (2021), 121082.
[23] V. Matkovic, G. Apseloff, D.R. Shepard, N. Gerber, Use of gallium to treat Paget's disease of bone: a pilot study, Lancet 335 (8681) (1990) 72–75.
[24] E. Verron, J.M. Bouler, J.C. Scimeca, Gallium as a potential candidate for treatment of osteoporosis, Drug Discov. Today 17 (19–20) (2012) 1127–1132.
[25] H. Lindgren, A. Sjöstedt, Gallium potentiates the antibacterial effect of gentamicin against francisella tularensis, Antimicrob. Agents Chemother. 60 (1) (2015) 288–295.
[26] A.B. Kelson, M. Carnevali, V.T. Le, Gallium-based anti-infectives: targeting microbial iron-uptake mechanisms, Curr. Opin. Pharmacol. 13 (5) (2013) 707–716.
[27] E. Verron, M. Masson, S. Khoshniat, L. Duplomb, Y. Wittrant, M. Baud'huin, Z. Badran, B. Bujoli, P. Janvier, J.C. Scimeca, J.M. Bouler, J. Guicheux, Gallium modulates osteoclastic bone resorption in vitro without affecting osteoblasts, Br. J. Pharmacol. 159 (8) (2010) 1681–1692.
[28] I.S. Geljic, I. Guberovic, B. Didak, H.S. Antomarchi, A.S. Alliana, F. Boukhechba, J. M. Bouler, J.C. Scimeca, E. Verron, Gallium, a promising candidate to disrupt the vicious cycle driving osteolytic metastases, Biochem. Pharmacol. 116 (2016) 11–21.
[29] F.P. He, C. Qiu, T.L. Lu, X.T. Shi, J.D. Ye, Conjunction of gallium doping and calcium silicate mediates osteoblastic and osteoclastic performances of tricalcium phosphate bioceramics, Biomed. Mater. 17 (1) (2021), 015012.
[30] A. Cochis, B. Azzimonti, C.D. Valle, E.D. Giglio, N. Bloise, L. Visai, S. Cometa, L. Rimondini, R. Chiesa, The effect of silver or gallium doped titanium against the multidrug resistant Acinetobacter baumannii, Biomaterials 80 (2016) 80–95.
[31] J.L. Krauss, P.M. Roper, A. Ballard, C.C. Shih, J.A. Fitzpatrick, J.E. Cassat, P.Y. Ng, N.J. Pavlos, D.J. Veis, *Staphylococcus aureus* infects osteoclasts and replicates intracellularly, mBio 10 (5) (2019) e02447-19.
[32] H.S. Wang, X. Li, Z.Y. Zhu, H.S. Wang, B. Wei, X.Z. Bai, Hydrogen sulfide promotes lipopolysaccharide-induced apoptosis of osteoblasts by inhibiting the AKT/NF-kB signaling pathway, Biochem. Biophys. Res. Commun. 524 (4) (2020) 832–838.
[33] Y.T. Wang, Y.H. Lin, C.Y. Cheng, P.Y. Chen, P. Zhang, H.T. Wu, K.Q. Li, Y. Deng, J. K. Qian, X.R. Zhang, B. Yu, NF-κB/TWIST1 mediates migration and phagocytosis of macrophages in the mice model of implant-associated *Staphylococcus aureus* osteomyelitis, Front. Microbiol. 11 (2020) 1301.
[34] T. Jin, P.J. He, R.R. Yang, R.Z. Geng, G.X. Yang, Y.Q. Xu, CHI3L1 promotes *Staphylococcus aureus*-induced osteomyelitis by activating p38/MAPK and Smad signaling pathways, Exp. Cell Res. 403 (1) (2021), 112596.
[35] N.E. Putnam, L.E. Fulbright, J.M. Curry, C.A. Ford, J.R. Petronglo, A.S. Hendrix, J. E. Cassat, MyD88 and IL-1R signaling drive antibacterial immunity and osteoclast-driven bone loss during *Staphylococcus aureus* osteomyelitis, PLoS Pathog. 15 (4) (2019), e1007744.
[36] M. Kurtjak, M. Vukomanović, L. Kramer, D. Suvorov, Biocompatible nano-gallium/hydroxyapatite nanocomposite with antimicrobial activity, J. Mater. Sci. Mater. Med. 27 (11) (2016) 170.
[37] V.B. Kumar, M. Natan, G. Jacobi, Z. Porat, E. Banin, A. Gedanken, Ga@C-dots as an antibacterial agent for the eradication of *Pseudomonas aeruginosa*, Int. J. Nanomed. 12 (2017) 725–730.

[38] S. Stankovich, D.A. Dikin, G.H. Dommett, K.M. Kohlhaas, E.J. Zimney, E.A. Stach, R.D. Piner, S.T. Nguyen, R.S. Ruoff, Graphene-based composite materials, Nature 442(7100) 282-286.
[39] X.Z. Xie, C.Y. Mao, X.M. Liu, Y.Z. Zhang, Z.D. Cui, X.J. Yang, K. Yeung, H.B. Pan, P. K. Chu, S.L. Wu, Synergistic bacteria-killing through photodynamic and physical actions of graphene oxide/Ag/collagen coating, ACS Appl. Mater. Interfaces 9 (31) (2017) 26417–26428.
[40] W.J. Zhang, Z.H. Li, Y. Liu, D.X. Ye, J.H. Li, L.Y. Xu, B. Wei, X.L. Zhang, X.Y. Liu, X. Q. Jiang, Biofunctionalization of a titanium surface with a nano-sawtooth structure regulates the behavior of rat bone marrow mesenchymal stem cells, Int. J. Nanomed. 7 (2012) 4459–4472.
[41] I. Wiegand, K. Hilpert, R.E.W. Hancock, Agar and broth dilution meth ods to determine the minimal inhibitory concentration (MIC) of antimicrobial substances, Nat. Protoc. 3 (2) (2008) 163–175.
[42] A.S. Abd-EI-Aziz, C. Agatemor, N. Etkin, D.P. Overy, M. Lanteigne, K. McQuillan, R.G. Kerr, Antimicrobial organometallic dendrimers with tunable activity against multidrug-resistant bacteria, Biomacromolecules 16 (11) (2015) 3694–3703.
[43] H.Y. Chen, M. Zhang, B.W. Li, D. Chen, X.Y. Dong, Y.H. Wang, Y.Q. Gu, Versatile antimicrobial peptide-based ZnO quantum dots for *in vivo* bacteria diagnosis and treatment with high specificity, Biomaterials 53 (2015) 532–544.
[44] Y. Yang, S.B. Yang, Y.G. Wang, S.H. Zhang, Z.F. Yu, T.T. Tang, Bacterial inhibition potential of quaternised chitosan-coated VICRYL absorbable suture: an *in vitro* and *in vivo* study, J. Orthop. Translat. 8 (2016) 49–61.
[45] Y. Yang, M. Li, H. Luo, D. Zhang, Surface-decorated graphene oxide sheets with copper nanoderivatives for bone regeneration: an *in vitro* and *in vivo* study regarding molecular mechanisms, osteogenesis, and anti-infection potential, ACS Infect. Dis. 8 (3) (2022) 499–515.
[46] Y. Yang, S. Yang, Y. Wang, Z. Yu, H. Ao, H. Zhang, L. Qin, O. Guillaume, D. Eglin, R.G. Richards, T. Tang, Anti-infective efficacy, cytocompatibility and biocompatibility of a 3D-printed osteoconductive composite scaffold functionalized with quaternized chitosan, Acta Biomater. 46 (2016) 112–128.
[47] S.H. Lin, G.Z. Yang, F. Jiang, M.L. Zhou, S. Yin, Y.M. Tang, T.T. Tang, Z.Y. Zhang, W.J. Zhang, X.Q. Jiang, A magnesium-enriched 3D culture system that mimics the bone development micro- environment for vascularized bone regeneration, Adv. Sci. 6 (12) (2019), 1900209.
[48] R. Ma, S.C. Tang, H.L. Tan, J. Qiao, W.T. Lin, Y.G. Wang, C.S. Liu, J. Wei, T. T. Tang, Preparation, characterization, *in vitro* bioactivity, and cellular responses to a polyetheretherketone bioactive composite containing nanocalcium silicate for bone repair, ACS Appl. Mater. Interfaces 6 (15) (2014) 12214–12225.
[49] M.S. Rahman, N. Akhtar, H.M. Jamil, R.S. Banik, S.M. Asaduzzaman, TGF-β/BMP signaling and other molecular events: regulation of osteoblastogenesis and bone formation, Bone Res 3 (2015), 15005.
[50] M. Nagasawa, L.F. Cooper, Y. Qgino, D. Mendonca, R. Liang, S. Yang, G. Mendonca, K. Uoshima, Topography influences adherent cell regulation of osteoclastogenesis, J. Dent. Res. 95 (3) (2016) 319–326.
[51] J. Wang, J. Xu, X. Wang, L. Sheng, L. Zheng, B. Song, G. Wu, R. Zhang, H. Yao, N. Zheng, M. Ong, P. Yung, L. Qin, Magnesium-pretreated periosteum for promoting bone-tendon healing after anterior cruciate ligament reconstruction, Biomaterials 268 (2021), 120576.
[52] M. Li, Y. Yang, Quaternized chitosan promotes the antiproliferative effect of vemurafenib in melanoma cells by increasing cell permeability, OncoTargets Ther. 11 (2018) 8293–8299.
[53] C.Y. Mao, Y.G. Wang, X. Zhang, X.Y. Zheng, T.T. Tang, E.Y. Lu, Double-edged-sword effect of IL-1β on the osteogenesis of periodontal ligament stem cells via crosstalk between the NF-κB, MAPK and BMP/Smad signaling pathways, Cell Death Dis. 7 (7) (2016), e2296.
[54] Y.H. Hu, J. Liu, J. Lu, P.X. Wang, J.X. Chen, Y. Guo, F.H. Han, J.J. Wang, W. Li, P. Q. Liu, sFRP1 protects H9c2 cardiac myoblasts from doxorubicin-induced apoptosis by inhibiting the Wnt/PCP-JNK pathway, Acta Pharmacol. Sin. 41 (9) (2020) 1150–1157.
[55] M. Li, Y. Liu, Y. Liu, L. Yang, Y. Xu, W. Wang, Z. Jiang, Y. Liu, S. Wang, C. Wang, Downregulation of GNA15 inhibits cell proliferation via P38 MAPK pathway and correlates with prognosis of adult acute myeloid leukemia with normal karyotype, Front. Oncol. 11 (2021), 724435.
[56] H. Kasperczyk, K.L. Ferla-Brühl, M.A. Westhoff, L. Behrend, R.M. Zwacka, K. M. Debatin, S. Fulda, Betulinic acid as new activator of NF-κB: molecular mechanisms and implications for cancer therapy, Oncogene 24 (46) (2005) 6945–6956.
[57] A.S. Abdelsattar, A. Dawound, M.A. Helal, Interaction of nanoparticles with biological macromolecules: a review of molecular docking studies, Nanotoxicology 15 (1) (2021) 66–95.
[58] O. Trott, A.J. Olson, AutoDock Vina, Improving the speed and accuracy of docking with a new scoring function, efficient optimization and multithreading, J. Comput. Chem. 31 (2) (2010) 455–461.
[59] H. Yang, B. Jia, Z. Zhang, X. Qu, G. Li, W. Lin, D. Zhu, K. Dai, Y. Zheng, Alloying design of biodegradable zinc as promising bone implants for load-bearing applications, Nat. Commun. 11 (1) (2020) 401.
[60] Y.F. Zhuang, L. Ren, S.Y. Zhang, X. Wei, K. Yang, K.R. Dai, Antibacterial effect of a copper-containing titanium alloy against implant-associated infection induced by methicillin- resistant *Staphylococcus aureus*, Acta Biomater. 119 (2021) 472–484.
[61] M.L. Bouxsein, S.K. Boyd, B.A. Christinasen, R.E. Guldberg, K.J. Jepsen, R. Müller, Guidelines for assessment of bone microstructure in rodents using micro-computed tomography, J. Bone Miner. Res. 25 (2010) 1468–1486.
[62] G. Zhang, B.S. Guo, H. Wu, T. Tang, B.T. Zhang, L.Z. Zheng, Y.X. He, Z.J. Yang, X. H. Pan, H. Chow, K. To, Y.P. Li, D.H. Li, X.L. Wang, Y.X. Wang, K. Lee, Z.B. Hou, N. Dong, G. Li, K. Leung, L. Huang, F.C. He, L.Q. Zhang, L. Qin, A delivery system targeting bone formation surfaces to facilitate RNAi-based anabolic therapy, Nat. Med. 18 (2) (2012) 307–314.
[63] M.S. Smeltzer, J.R. Thomas, S.G. Hickmon, R.A. Skinner, C.L. Nelson, D. Griffith, T. R. Parr Jr., R.P. Evans, Characterization of rabbit model of staphylococcal osteomyelitis, J. Orthop. Res. 15 (3) (1997) 414–421.
[64] X.W. Wang, Q.Q. Shi, Z.B. Zha, D.D. Zhu, L.R. Zheng, L.X. Shi, X.W. Wei, L. Lian, K. L. Wu, L. Cheng, Copper single-atom catalysts with photothermal performance and enhanced nanozyme activity for bacteria-infected wound therapy, Bioact. Mater. 6 (12) (2021) 4389–4401.
[65] J.L. Bourque, M.C. Biesinger, K.M. Baines, Chemical state determination of molecular gallium compounds using XPS, Dalton Trans. 45 (18) (2016) 7678–7696.
[66] B.N. Ganguly, V. Verma, D. Chatterjee, B. Satpati, S. Debnath, P. Saha, Study of gallium oxide nanoparticles conjugated with β-cyclodextrin: an application to combat cancer, ACS Appl. Mater. Interfaces 8 (27) (2016) 17127–17137.
[67] K. Wang, J. Ruan, H. Song, J.L. Zhang, Y. Wo, S.W. Guo, D.X. Cui, Biocompatibility of graphene oxide, Nanoscale Res. Lett. 6 (1) (2011) 8.
[68] K. Pajor, Ł. Pajchel, A. Zgadzaj, U. Piotrowska, J. Kolmas, Modifications of hydroxyapatite by gallium and silver ions-Physicochemical characterization, cytotoxicity and antibacterial evaluation, Int. J. Mol. Sci. 21 (14) (2020) 5006.
[69] S. Ghosh, K. Chatterjee, Poly (ethylene glycol) functionalized graphene oxide in tissue engineering: a review on recent advances, Int. J. Nanomed. 15 (2020) 5991–6006.
[70] M. Wang, Y. Yang, G. Chi, K. Yuan, F. Zhou, L. Dong, H. Liu, Q. Zhou, W. Gong, S. Yang, T. Tang, A 3D printed Ga containing scaffold with both anti-infection and bone homeostasis-regulating properties for the treatment of infected bone defects, J. Mater. Chem. B 9 (23) (2021) 4735–4745.
[71] F. Kurtuldu, N. Mutlu, A.R. Boccaccini, D. Galusek, Gallium containing bioactive materials: a review of anticancer, antibacterial, and osteogenic properties, Bioact. Mater. 17 (2022) 125–146.
[72] J.M. Wagner, H. Jaurich, C. Wallner, S. Abraham, M. Becerikli, M. Dadras, K. Harati, V. Duhan, V. Khairnar, M. Lehnhardt, B. Behr, Diminished bone regeneration after debridement of posttraumatic osteomyelitis is accompanied by altered cytokine levels, elevated B cell activity, and increased osteoclast activity, J. Orthop. Res. 35 (11) (2017) 2425–2434.
[73] K. Xie, N. Wang, Y. Guo, S. Zhao, J. Tan, L. Wang, G. Li, J. Wu, Y. Yang, W. Xu, J. Chen, W. Jiang, P. Fu, Y. Hao, Additively manufactured biodegradable porous magnesium implants for elimination of implant-related infections: an *in vitro* and *in vivo* study, Bioact. Mater. 8 (2021) 140–152.
[74] W.C. Kenry, K.P. Lee, C.T. Loh, Lim, When stem cells meet graphene: opportunities and challenges in regenerative medicine, Biomaterials 155 (2018) 236–250.
[75] S.A. Zhang, K. Yang, L.Z. Feng, Z. Liu, *In vitro* and *in vivo* behaviors of dextran functionalized graphene, Carbon 49 (12) (2011) 4040–4049.